RESEARCH ARTICLE

Key Points:
- Deformation experiments on single crystals of K-feldspar
- Brittle fracturing and partial melting intimately related
- Fine-grained gouges deform by dissolution-precipitation creep

Correspondence to:
M. Negrini,
marianne.negrini@uit.no

Semibrittle deformation and partial melting of perthitic K-feldspar: An experimental study

Marianne Negrini[1], Holger Stünitz[1], Pritam Nasipuri[2], Luca Menegon[3], and Luiz F. G. Morales[4]

[1]Institute of Geology, University of Tromsø, Tromsø, Norway, [2]Department of Earth and Environmental Sciences, Indian Institute of Science Education and Research, Bhopal, India, [3]School of Geography, Earth and Environmental Sciences, Plymouth University, Plymouth, UK, [4]Deutsches GeoForschungsZentrum, Potsdam, Germany

Abstract To investigate the relationships between deformation, cracking, and partial melting in the lower continental crust, axial compression and hydrostatic experiments were performed on K-feldspar single crystals at temperatures of 700° and 900°C and confining pressures between 0.75 and 1.5 GPa. Sample deformation was carried out at a constant strain rate of $\sim 10^{-6}\,s^{-1}$. The samples deformed at 700°C show typical brittle behavior with formation of conjugate fractures and peak stresses that increase with confining pressure. Samples deformed at 900°C show formation of shear fractures, peak stresses below the Goetze criterion, and inverse confining pressure dependence of peak stress, indicating that along the fractures deformation was not dominantly friction controlled. Microstructural and chemical analyses reveal the presence of melt ($<$6 vol %) of inhomogeneous composition along the shear zones and chemical compositional changes of gouge fragments. In a hydrostatic experiment performed at 900°C, no melt and no compositional changes were observed. These observations indicate that deformation of K-feldspars at high pressures and temperatures is controlled by the simultaneous formation of brittle fractures and melt. The formation of melt is strongly accelerated and kinetically favored by cracking, as demonstrated by the absence of melting in the hydrostatic experiments. However, the melt along fractures does not dramatically weaken the samples, as the melt domains remain isolated during deformation. The fine-grained gouge fragments formed along the fracture systems undergo chemical homogenization. The dominant deformation mechanism in the gouge is likely to be melt-enhanced diffusion creep, which may also assist the chemical homogenization process.

1. Introduction

The relationships between deformation and melting have attracted extensive interest because of their fundamental influence on crustal rheology. The presence of melt has a tremendous effect on the mechanics and rheology of rock and therefore controls a range of both large and small-scale tectonic processes [e.g., *Davidson et al.*, 1994; *Clark and Royden*, 2000; *Beaumont et al.*, 2001; *Royden et al.*, 2008; *King et al.*, 2010, 2011]. Similarly, deformation influences the melting process, both in terms of the grain-scale distribution of melt in polycrystalline aggregates, and the segregation and extraction of melt in partially molten continental crust and mantle rocks [e.g., *Cooper*, 1990; *Bussod and Christie*, 1991; *Brown*, 1994, 2007; *Collins and Sawyer*, 1996; *Kohlstedt and Zimmerman*, 1996; *Weinberg*, 1999; *Zimmerman et al.*, 1999; *Sawyer*, 2001; *Marchildon and Brown*, 2002; *Holtzman et al.*, 2003a, 2003b; *Parsons et al.*, 2004; *Kohlstedt et al.*, 2009].

Since the late 1970s, laboratory experiments have demonstrated a close relationship between rock strength and melt content [e.g., *Arzi*, 1978; *Rutter and Neumann*, 1995; *Mecklenburgh and Rutter*, 2003; *Scott and Kohlstedt*, 2006; *Takei and Holtzman*, 2009]. *Rosenberg and Handy* [2005] reported dramatic weakening (strength loss of about 80%) at a melt fraction of 0.07, caused by the onset of melt interconnectivity. At that low melt fraction, however, the bulk stress was still supported by the solid framework. The breakdown of the solid framework occurs at a melt fraction between 0.1 and 0.3 which produces a second pronounced weakening [*Arzi*, 1978; *van der Molen and Paterson*, 1979; *Wickham*, 1987].

The distribution of melt in a rock also has a great influence on rheological behavior [*Cooper et al.*, 1989; *Kohlstedt*, 1992]. Melt films that are spread along grain boundaries provide high-diffusivity pathways that can drastically enhance creep rates [*Pharr and Ashby*, 1983; *Jin et al.*, 1994; *Hirth and Kohlstedt*, 1995a, 1995b], whereas melt confined to grain triple junctions may result in only moderate enhancements of the diffusion creep rate [*Cooper and Kohlstedt*, 1984b; *Dimanov et al.*, 1998]. In addition, melt may influence the main deformation mechanisms of the rock. Experimental deformation of partially molten granitic aggregates

suggests a switch from dislocation creep to predominantly melt-enhanced diffusion creep with increasing melt fraction [*Dell'Angelo et al.*, 1987; *Dell'Angelo and Tullis*, 1988].

Field observations indicate that localization of deformation into melt-weakened zones in the continental crust plays an important role in the formation of orogens and mountain belts [*Davidson et al.*, 1994; *Beaumont et al.*, 2001; *Slagstad*, 2005; *Schulmann et al.*, 2008; *Lexa et al.*, 2011]

The spatial distribution of melt in a rock and the segregation and migration of melt in partially molten crust are dependent on the applied forces and on the regional stress field [*Brown*, 1994, 2007, 2010; *Davidson et al.*, 1994; *Kohlstedt and Zimmerman*, 1996; *Daines and Kohlstedt*, 1997; *Zimmerman et al.*, 1999; *Rosenberg and Handy*, 2001; *Zimmerman and Kohlstedt*, 2004; *King et al.*, 2010; *Kohlstedt and Holtzman*, 2009]. Shear stresses cause the segregation of melt from grain boundaries where it was originally formed, producing aligned melt domains distributed within melt-laden shear bands [e.g., *Holtzman and Kohlstedt*, 2007]. Furthermore, deformation leads to the migration of melt from high-angle bands toward bands oriented at a lower angle to the main compression direction [*Holtzman and Kohlstedt*, 2007]. Many natural examples of melt segregation and melt extraction controlled by deformation and tectonic stress fields have been reported [e.g., *Vigneresse*, 1995a, 1995b; *Collins and Sawyer*, 1996; *Brown and Solar*, 1998; *Weinberg*, 1999].

The relationships between deformation and partial melting are especially important in terms of the rheological behavior of the lower crust, where pressure-temperature (P-T) conditions are often high enough for partial melting to occur. In order to gain insights into the deformation behavior of partially molten continental crust, we performed deformation experiments on natural perthitic single crystals of K-feldspar. Feldspar was chosen in this case because it is a very common mineral in the continental crust. The quartz-free assemblage K-feldspar + plagioclase has a higher melting temperature than granitic compositions (containing quartz), so this system has advantages in experimental deformation studies where crystal plastic deformation and melting effects are to be studied. In addition, there are few experimental studies [*Tullis and Yund*, 1977; *Willaime et al.*, 1979] on the deformation behavior of K-feldspars at high pressures and temperatures.

The experiments were performed with a solid medium deformation apparatus at pressures and temperatures where feldspar is expected to undergo partial melting (above the solidus temperature) and deform predominantly by crystal-plastic deformation mechanisms. The experiments were designed to study the relationships between cracking and partial melting and to understand the influence these processes have on the chemical and mechanical properties of the material.

2. Methods of Study

2.1. Starting Materials

Two different natural K-feldspar single crystals were used (Figure 1): (a) a pink variety and (b) a white variety. The chemical composition of the different phases is given in Table 1.

The pink perthitic K-feldspar crystal (Figure 1a) contains 84% K-feldspar ($Ab_{06}An_0Or_{94}$), 15% albite ($Ab_{98}An_{1.5}Or_{0.5}$), and volumetrically insignificant white mica (0.5%) and quartz (0.2%). The pink K-feldspar contains a small amount of H_2O. In a sample heated to 1000°C for 2 h we determined a H_2O content of ~0.1 wt % (by loss on ignition). The H_2O is assumed to be present in fluid inclusions, cleavage cracks, white mica, and some adsorbed H_2O.

The mineral appears uniform in color in hand specimen, but three distinct sets of albite exsolution lamellae are observed under the light microscope (Figure 1a): (i) The main set of lamellae is oriented at 10–20° to the {100} plane. These lamellae, which have a width up to 250 μm and length in the millimeter range, are often twinned, following the albite twin law. The thicker lamellae have sharp boundaries and locally open up in pockets containing small quartz grains. (ii) Small perthite lamellae (stringlets type after *Alling* [1938]) of 10–30 μm in width and up to 200 μm in length are oriented dominantly parallel to the {100} plane (Figure 1a). This set of lamellae is inhomogeneously distributed in the rock: lamellae-rich regions alternate with perthite-free regions. (iii) Short perthite lamellae with poorly defined boundaries are oriented parallel to the {010} direction (Figure 1a). These are typically 30–60 μm wide and terminate at the contacts with the main set of lamellae but never crosscut them.

Polysynthetic twinning is pervasively and homogeneously distributed throughout the whole K-feldspar matrix. The twinning occurs in two sets (albite and pericline law) [*Smith and Brown*, 1988], which intersect
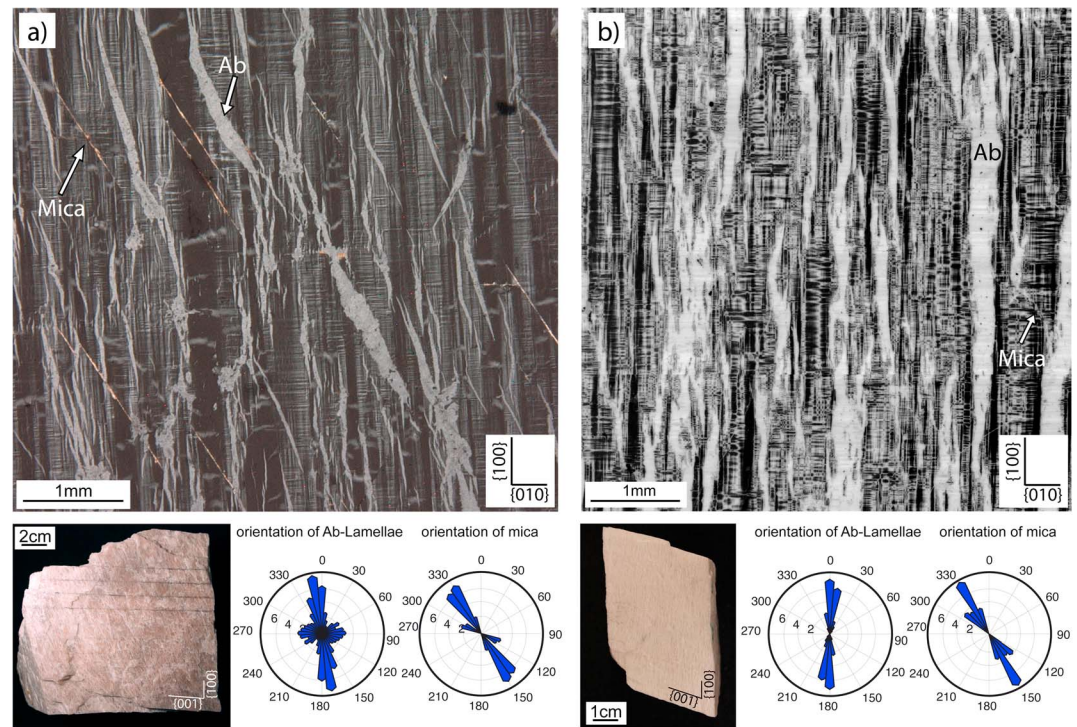
Figure 1. Characterization of the two starting materials. (a) Pink K-feldspar and (b) white K-feldspar. Specimens were cored normal to the {010} plane. Both crystals contain albite lamellae, oriented mica grains (30° to the {100} plane), and two sets of twins (albite and pericline laws). The rose diagrams show a large number of small perthite lamellae oriented approximately parallel to the {100} plane in both crystals. The pink K-feldspar (Figure 1a) contains some coarse albite lamellae oriented at 35° to {100} and shorter albite lamellae oriented parallel to {010}.

approximately at right angles and form a quadrille structure (cross-hatched twinning) [*Fitz Gerald and McLaren*, 1982; *Smith and Brown*, 1988; *Putnis*, 2002]. Thin (10 μm) and up to 700 μm long white mica domains are oriented at 30–40° to {010} corresponding to the {110} cleavage plane of the feldspar (Figure 1a).

The white perthitic K-feldspar (Figure 1b) contains 81% K-feldspar with a composition $Ab_{11}Or_{89}An_0$ and 19% albite lamellae ($Ab_{98}An_{01}Or_{01}$) (Table 1). Very little white mica and quartz are contained in this material. Loss on ignition measurements indicates for this material a water content of ~0.2 wt %. The specimen shows similar macroscopic and microscopic characteristics to the pink K-feldspar. The major differences are the

Table 1. Chemical Compositions (Determined From EMPA Analyses) of the Two Feldspar Single Crystals Used as Starting Material[a]

	Pink K-Feldspar			White K-Feldspar	
Fase	Matrix (K-Fsp)	Ab-Lamellae	Mica	Matrix (K-Fsp)	Ab-Lamellae
SiO_2	64.74	67.65	43.92	64.79	69.02
Al_2O_3	18.71	19.77	35.78	17.85	19.87
FeO	0.00	0.00	1.61	0.46	0.01
CaO	0.00	0.36	0.01	0.03	0.18
Na_2O	0.68	11.73	0.49	1.25	12.06
MgO	0.00	0.00	0.04	0.00	0.00
K_2O	15.70	0.08	10.59	15.25	0.16
MnO	0.06	0.00	0.01	0.00	0.00
Total	99.90	99.59	92.44	99.62	101.30
Ab (%)	6.20	97.88		11.02	98.31
An (%)	0.00	1.66		0.13	0.82
An (%)	93.80	0.46		88.85	0.85

[a]Measurements are given in wt %.

following: (i) The twin density in the white K-feldspar is higher, with shorter and thinner albite and pericline twins. (ii) The inhomogeneously distributed white mica forms shorter and thinner domains oriented at ~30° to the {100} cleavage planes in the white K-feldspar. (iii) The main set of albite exsolution lamellae of the white K-feldspar does not form pockets containing quartz. Instead, small (30–60 μm) quartz crystals are distributed along the boundaries of the albite lamellae. Occasionally, the small quartz crystals form aggregates around 50 μm in size. (iv) Slightly more porosity is found along the albite lamellae/K-feldspar boundaries. (v) The set of albite exsolution lamellae oriented parallel to the {010} plane is missing.

2.2. Sample Preparation

Two different types of samples were prepared: (i) cylindrical samples for axial compression and hydrostatic experiments and (ii) powder samples for hydrostatic experiments.

The orientation of the crystals was determined macroscopically using the geometry of the well-developed crystal planes and the orientation of the albite lamellae. All cylindrical samples, which had a length of 10–12 mm and a diameter of 6.3 mm, were cored normal to the {010} plane of the crystals (hard orientation for slip). The samples were air dried at 120°C and wrapped in Ni foil prior to inserting them into the can-shaped Pt jackets and weld sealing. In samples with H_2O added, 0.1–0.2 μL distilled water (corresponding to 0.1–0.2 wt %) was introduced using a micropipette to the lower part of the capsule, beneath the sample, in order to reduce potential evaporation of the water during the subsequent welding process at the top part of the capsule. Evaporation of the water during the welding process was further impeded by using a millisecond welding time of a point-welding device (Lampert) in order to minimize heating of the sample and jacket.

For the powder experiments the K-feldspar starting material was ground in an agate mortar. The powder fraction with a grain size of 12–20 μm was obtained by sieving the ground rock through a series of paper filters and subsequently drying the powders at 110°C. The 0.1 g powder was placed between 45° precut alumina-forcing blocks inside a Ni foil and weld-sealed Pt jacked (we used this sample geometry because deformation experiments were also carried out with powder. In order to have the same temperature gradient in both types of experiment we used the same sample assembly.). No H_2O was added to the feldspar powder but, based on measurements of *Stünitz and Tullis* [2001] on similar powders, we assume between ~0.1 and 0.2 wt % of adsorbed H_2O.

2.3. Experimental and Analytical Procedures

The two different types of experiments (axial compression and hydrostatic) were performed in a modified Griggs-type solid medium deformation apparatus [*Tullis and Tullis*, 1986]. In all experiments NaCl was used as the confining medium, and alumina was used for the outer pistons. The temperature was monitored with a Pt-Pt10%Rh S-type thermocouple placed in the middle of the sample along the outer margin. Double thermocouple experiments, in which one thermocouple was placed in the center and the other at the contact between forcing block and outer piston, indicate a maximum temperature difference of ~4–5% from the center to the end of the shear zone (a distance of ~3 mm).

For each experiment the hydrostatic conditions (temperatures of 700–900°C and pressures of 0.75–1.5 GPa) were typically reached in 6 h or less by a stepwise increase of confining pressure and temperature. Once the desired conditions were reached, the samples were deformed by advancing the σ_1 piston at a corresponding axial strain rate of ~10^{-6} s^{-1} up to a maximum axial shortening of 40%. At the end of the experiments the motor was stopped and the samples immediately quenched to 200°C. Subsequently, pressure and load were slowly decreased to atmospheric conditions in order to minimize the formation of unloading fractures.

The hydrostatic experiments were carried out at 900°C and 1.0 GPa in the same way as for axial compression experiments. The samples were held at hydrostatic conditions for 71 h, corresponding to the period of time necessary to reach 35% strain in an axial compression experiment. After the hydrostatic heat treatment the samples were quenched and slowly depressurized to atmospheric conditions. The conditions of all the experiments are summarized in Table 2. The force and displacement data recorded during each experiment were processed using the MATLAB program RIG by Matej Pec (http://sites.google.com/site/rigprogram/).

After deformation the samples were cut normal to the (often conjugate) set of planes accommodating the main displacements during deformation (the same orientation was used for the hydrostatic experiments). This section orientation is always normal to the {100} plane. The cut surfaces were impregnated with epoxy

Table 2. Summary of Deformation Conditions of All Performed Experiments (Pc = Confining Pressure, T = Temperature, $\dot{\varepsilon}$ = Strain Rate, t = Total Time at Pc and T)

Sample	Pc (GPa)	T (°C)	$\dot{\varepsilon}$ ($\times 10^{-6}$ s^{-1})	Total Time (h)	Strain (%)	Experiment Type	Starting Material	Water Added
216	1.00	900	2.1	48	33	Axial compression	White K-Fsp	As Is
218	1.00	900	1.6	44	9	Axial compression	White K-Fsp	0.2 wt %
221	1.00	900	1.3	38	15	Axial compression	White K-Fsp	0.1 wt %
222	1.00	900	1.2	69	23	Axial compression	Pink K-Fsp	As Is
223	1.00	900	1.3	89	36	Axial compression	Pink K-Fsp	0.1 wt %
250	1.50	900	1.8	50	25	Axial compression	Pink K-Fsp	As Is
258	0.75	900	1.4	76	28	Axial compression	Pink K-Fsp	As Is
265	1.00	900	0	95	0	Hydrostatic	Pink K-Fsp	As Is
267	1.00	900	0	42	0	Hydrostatic	Pink K-Fsp	Powder
271	1.00	900	0	71	0	Hydrostatic	Pink K-Fsp	As Is
276	1.50	900	1.5	87	35	Axial compression	Pink K-Fsp	As Is
292	1.00	900	1.1	37	3	Peak strength	Pink K-Fsp	As Is
293	0.75	900	1.1	44	2	Peak strength	Pink K-Fsp	As Is
294	0.75	900	1.1	32	3	Peak strength	Pink K-Fsp	As Is
295	0.75	900	1.2	68	18	Axial compression	Pink K-Fsp	As Is
296	1.50	900	1.6	93	30	Axial compression	Pink K-Fsp	As Is
297	1.50	900	1.2	41	2	Peak strength	Pink K-Fsp	As Is
298	1.00	700	1.1	89	21	Axial compression	Pink K-Fsp	As Is
300	0.75	700	1.3	41	12	Axial compression	Pink K-Fsp	As Is

and standard-polished petrographic thin-sections with a thickness of 30 µm were prepared. Examination of the samples was conducted using light as well as scanning electron (SEM) microscopy.

Backscattered imaging (BSE image) was carried out using a field-emission Philips XL30 SEM with an energy-dispersive X-ray detector (ZMB, Basel) and a ZEISS EVO50 (University of Bern). The images were taken at a beam current of 15 nA and an acceleration voltage of 20 kV. Quantitative element analyses were performed with a JEOL Superprobe 8200X (University of Copenhagen and ETH Zürich) at 15 kV and 20 nA, using a spot size of 5 µm. Compositions of the melt phase, which commonly is unstable under normal beam settings, were measured with a low-beam current of 10–12 nA, a spot-size of 10–12 µm, and counting time <10 s in order to avoid significant Na and H_2O loss.

Crystallographic preferred orientation (CPO) data were collected using the electron backscatter diffraction (EBSD) method [*Adams et al.*, 1993] in a FEI-Quanta 3-D field emission gun-focused ion beam scanning electron microscope equipped with an EDAX-TSL Digiview IV EBSD detector and TSL software OIM 5.31 at the Deutsches GeoForschungsZentrum-Potsdam. The samples were polished using standard methods with diamond pastes of different grain sizes down to 0.25 µm and chemically polished using a soft cloth and an alkaline solution of colloidal silica [*Flynn and Powell*, 1988] for 2 h. The EBSD analyses were conducted under low vacuum (10 Pa of H_2O) on an uncoated sample using 15 kV accelerating voltage, 8 nA beam current, 12 mm working distance, step size of 1 µm, and 70° sample tilt. The acquired diffraction patterns for the chemically homogenized feldspar grains (high-temperature monoclinic structure) were indexed using the crystallographic data for sanidine. The standardization of the confidence index (CI) of different points and CI correlation between neighboring points were carried as filtering procedures, and only data with CI > 0.2 were considered in the pole figures, which were plotted using one point per grain.

The phase distribution and melt fraction formed in the specimens were estimated from SEM images processed with Adobe Photoshop and Image SXM (www.liv.ac.uk/~sdb/ImageSXM/) as well as a number of macros developed by Renee Heilbronner (http://pages.unibas.ch/earth/micro/index.html). Melt domains were recognized in backscattered electron images (BSE) by means of their characteristic morphology, the presence of spherical fluid bubbles, and by the low contrast in comparison with other phases.

3. Results

### 3.1. Melt and Solid Compositions in the System Albite-Orthoclase-H_2O

In experiments, H_2O-saturated melting of alkali feldspars commences at 675° to 750°C at 1 GPa [*Luth et al.*, 1964; *Morse*, 1970; *Johannes and Holtz*, 1996]. There is a negative temperature dependence with increasing pressure for initial melt formation (solidus curve) during H_2O-saturated melting.
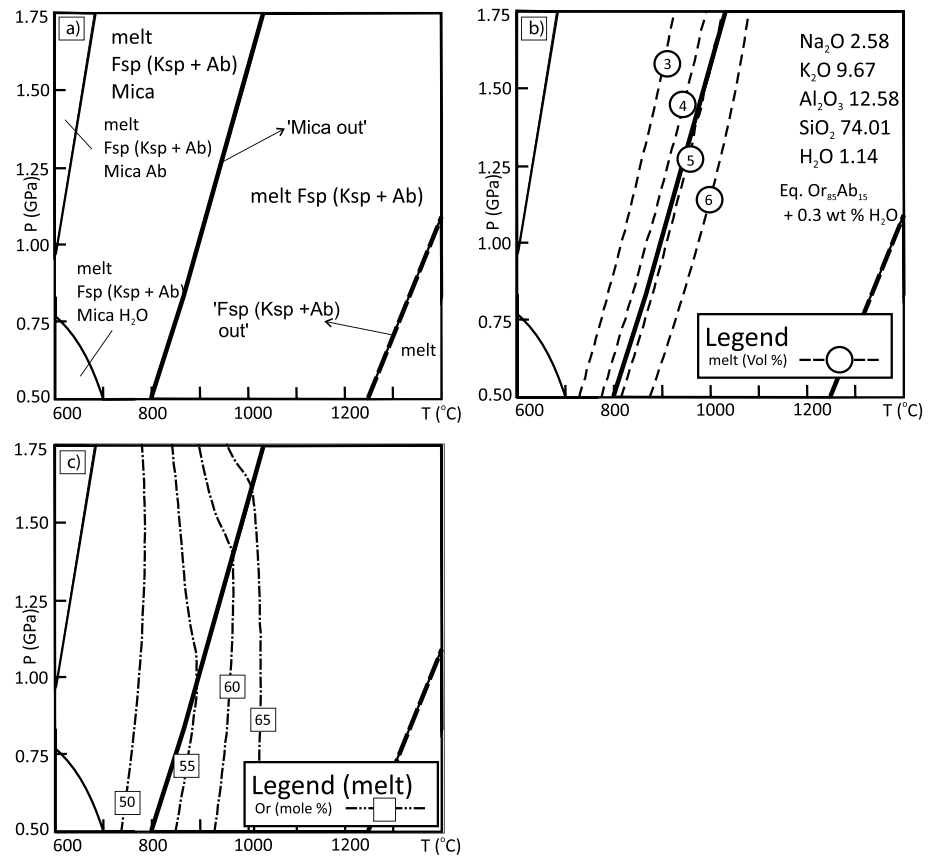
Figure 2. P-T pseudosection for the system Ab-Or-H_2O. (a) Phase topology of sanidine (Ksp + Ab), mica, and melt. (b) Calculated volume isoplate of the formed melt. Thermodynamic data predict at 1.0 GPa and 900°C a melt volume of around 5 wt %. (c) Expected composition of the formed melt.

The phase diagrams for the H_2O present melting of alkali feldspar (Na-K binary feldspar) have been modeled in the NKASH system (Figure 2) using PerpleX_07 [*Connolly*, 2009]. The reintegrated composition of the pink perthite single crystal has been used for calculations. The following solution models have been used for the pseudosection calculation (refer to the solution_model.dat file for details): mica [*Coggon and Holland*, 2002], melt [*Holland and Powell*, 1998], and for san (sanidine) [*Thompson and Waldbaum*, 1969]. The CORK model [*Holland and Powell*, 1998] was used as fluid equation of state for H_2O. The diagrams have been calculated using an upper estimated H_2O content of 0.3 wt %. The H_2O content represents the upper limit for the powder experiment, where, in addition to the ~0.1 wt % H_2O contained in the perthite crystal (in the form of white mica, fluid inclusions, and some adsorbed H_2O), an additional maximum of 0.2 wt % H_2O is assumed for the adsorption of H_2O to the powder [*Stünitz and Tullis*, 2001]. The additional adsorbed H_2O does not apply to the single-crystal samples as the surface area of those is not large so that ~0.1 wt % is taken as the H_2O content of the single-crystal samples (without H_2O added) and ~0.3 wt % as the H_2O content of the powder sample and the H_2O-added single-crystal samples.

The amount of total melt expected to be produced at the maximum estimated H_2O content of 0.3 wt % is just below 5 vol %, corresponding to ~4.8 wt % (Figure 2b), and the melt composition is expected to be ~ Or_{55} (Figure 2c). Considering the maximum temperature gradient in the samples, the melt content in cooler regions of the samples could be up to 1 wt % lower. During the melt-forming reaction, a solid single-phase feldspar is expected to form with a composition of $Or_{80}Ab_{20}$. The amount of melt increases with an increase of H_2O content in the system and decreases with pressure (Figures 2a and 2b) because of the increased solubility of H_2O in the melt with increasing pressure [e.g., *Johannes and Holtz*, 1996]. It should be emphasized that the amount of melt calculated is more or less within the error range of the accuracy of the
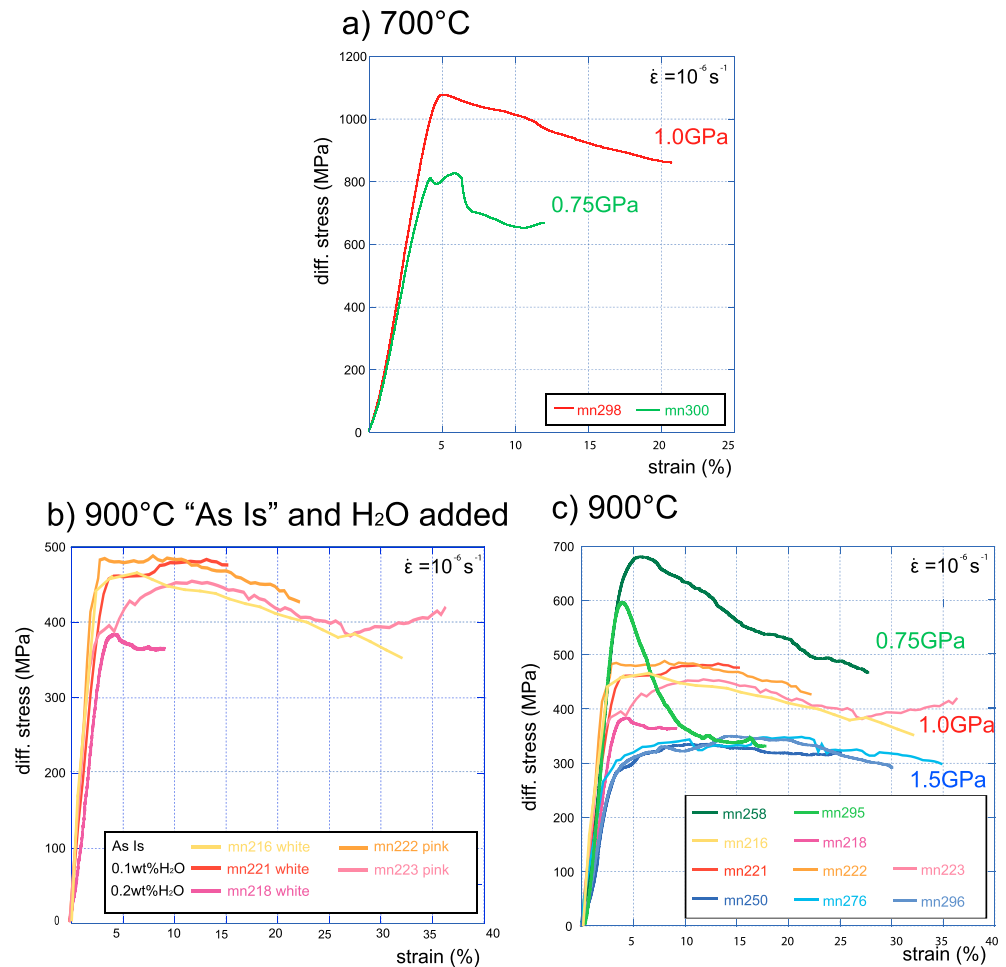
Figure 3. Stress-strain diagrams for K-feldspar deformed at different confining pressures and temperatures at a strain rate of ~1×10^{-6} s^{-1}. (a) Experiments at 700°C and confining pressure of 0.75 GPa (green) and 1.0 GPa (red). Samples were deformed as is. (b) Samples deformed as is and with added H_2O (0.1 and 0.2 wt %) do not show systematically different strengths at 900°C, 1.0 GPa confining pressure. (c) White K-feldspar (216, 218, and 221) and pink K-feldspar (all others) deformed at 900°C and confining pressure of 0.75 GPa (green), 1.0 GPa (red-yellow), and 1.5 GPa (blue). Note that there is no systematic strength difference between the two starting materials.

thermodynamic modeling (3–5%). Together with the compositions of the melt and solid phases, the calculated diagrams only serve to discuss the phase relationships in a semiquantitative way.

3.2. Mechanical Data

The stress-strain curves from experiments are shown in Figure 3. A series of experiments performed at 900°C on the pink and white perthitic K-feldspars show no systematic strength differences between the two different sample materials (Figure 3b). Furthermore, the addition of 0.1 wt % H_2O does not systematically change the mechanical behavior with respect to "as is" samples (Figures 3b and 3c). The addition of 0.2 wt % H_2O (the highest amount added, only to one sample, Table 2) results in a lower strength of the K-feldspar, so that subsequently samples were deformed without addition of H_2O in order to avoid potential pore pressure effects and variability due to different H_2O contents. As there is no systematic difference in mechanical behavior, all samples are described in the following text without differentiating between as is, water added, and pink or white perthite.

At 700°C (Figure 3a, close to the solidus temperature, no melt present) the crystals show peak stresses ~10% above the confining pressure values. After peak stress, at ~5% strain, there is a clear weakening of at least 10% in differential stress. The peak strength increases with increasing confining pressure (Figure 3a). This
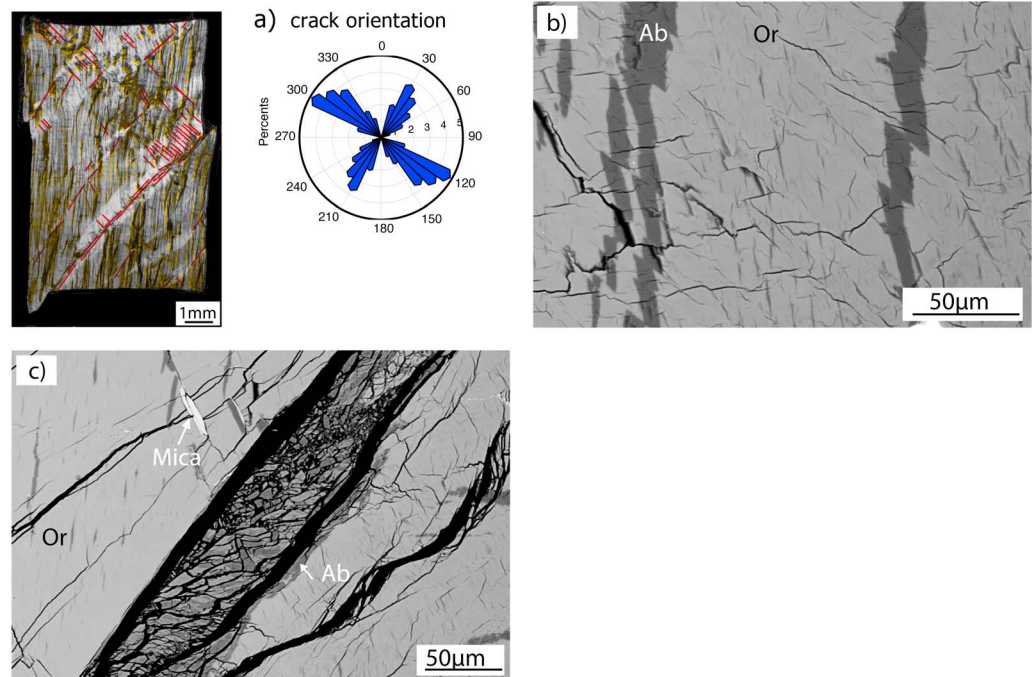
Figure 4. Microstructure of K-feldspar deformed as is at 700°C and confining pressure of 1.0 GPa. Compression direction is vertical in all figures. (a) Cross-polarized light micrograph of the deformed sample. Red lines mark the cracks, whose orientations are represented by the rose diagram on the right. Albitic lamellae are colored in yellow. (b) SEM backscatter image (BSE) showing extensive cracking in the deformed samples. The albitic lamellae are displaced by very small shear cracks oriented at 50° to the compression direction. Subhorizontal cracks are interpreted as unloading cracks forming during decompression of the sample after deformation. (c) SEM backscatter image (BSE) of a fault gouge along the major through-going shear fracture. Note that the fine-grained fragments have two different composition (dark material = albite (Ab), lighter part = K-feldspar (Or)).

behavior, i.e., strength above the confining pressure values and the positive dependence of peak stress on confining pressure, is characteristic of brittle deformation.

The samples deformed at 900°C (Figure 3c) show, after 5% strain, flow stresses of 30 to 70% of the confining pressure values. In all 900°C experiments, there is a clear dependence of flow stress on confining pressure: samples deformed at confining pressure (Pc) = 0.75 GPa show a peak strength 20–30% higher (600–680 MPa) than at 1.0 GPa confining pressure, and 60–80% higher than at 1.5 GPa confining pressure. Samples deformed at 1.5 GPa confining pressure attain the lowest flow stresses (330 MPa, steady state) after ~7% strain, while the 1.0 GPa confining pressure experiments show intermediate flow stresses (390–480 MPa). The degree of weakening is highest at low confining pressure, whereas at 1.5 GPa there is no weakening but more or less steady state flow (Figure 3c). Sample 295 (deformed at 0.75 GPa) weakened to the stress levels of the 1.5 GPa experiments after ~10% strain. Thus, with increasing confining pressure at 900°C, both the peak and flow stresses decrease, and weakening becomes less pronounced.

3.3. Microstructural Observations
3.3.1. Samples Deformed at 700°C
Experiments performed on K-feldspar single crystals at 700°C show microstructures typical of brittle deformation (Figure 4). The sample deformed at 1.0 GPa shows extensive cracking distributed throughout the whole sample. Major through-going and local shear cracks develop at 45–55° to the compression direction (Figure 4a). The sharp and distinct through-going shear cracks are surrounded by 0.5 mm wide regions with patchy undulatory extinction and different extinction angles (lattice rotation ~15°; Figure 4a). The lattice rotation is accommodated by closely spaced (few micrometers) fractures, which occur in the region around major cracks. These observations are similar to those made by *Tullis and Yund* [1987] in experimentally deformed plagioclase.
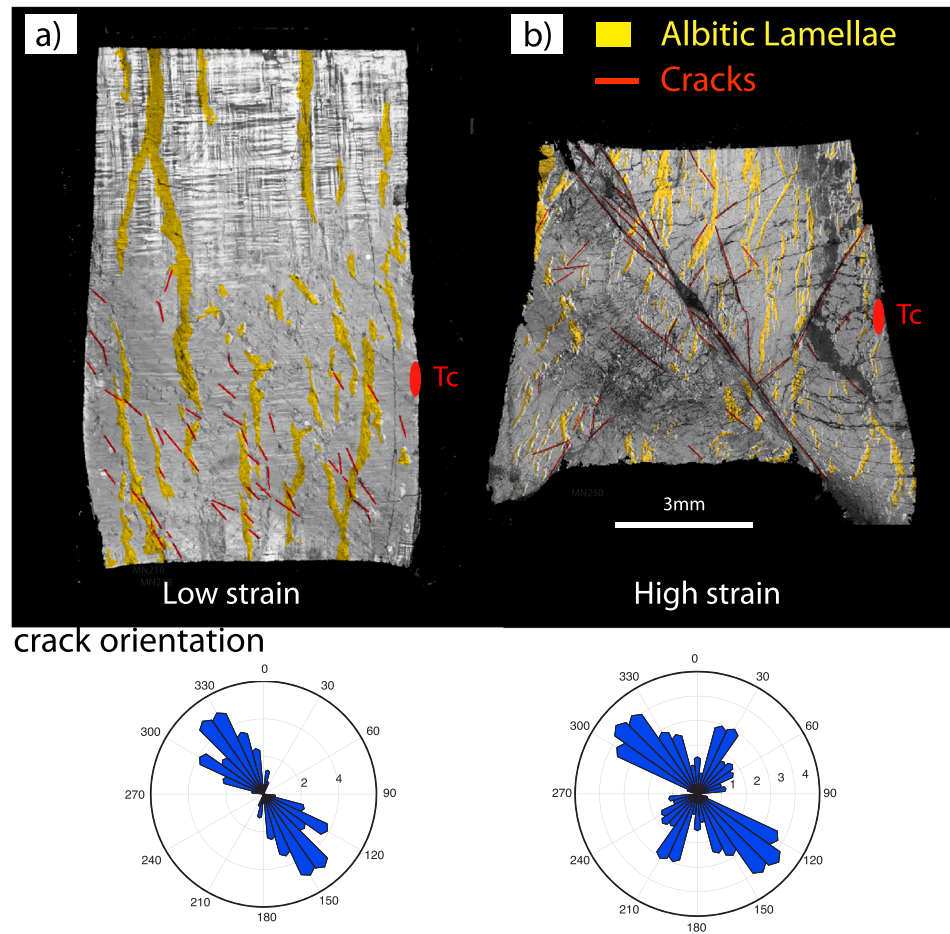
Figure 5. Light micrographs (crossed polarized) of deformed samples, showing the distribution and types of brittle features formed at (a) low and (b) high strain. Albite lamellae are colored in yellow and cracks in red. The final position of the Thermocouple (Tc) is also marked. The rose diagrams show the orientation of the cracks with respect to the axial shortening direction (vertical in all figures). (a) White K-feldspar (218) deformed with 0.1 wt % H_2O added, at 900°C, 1.0 GPa up to 9% strain. Short parallel cracks are oriented at 30–50° to σ_1. The deformation is concentrated in the lower part of the sample, where the temperature was highest during deformation. A pink K-feldspar sample (250) deformed at 900°C, 1.5 GPa up to 25% strain (Figure 5b). Cracking is concentrated along a through-going deformation zone oriented at 50° to σ_1. Asymmetric conjugate shear cracks, which develop mainly in the central part of the sample, are oriented at an angle of 30–60° to the main compression direction. Displacement along the cracks is well visible by the relative position of the displaced albite lamellae.

Fractures form conjugate sets enclosing an angle of ~80° (Figure 4a) and displace the twins and the albitic lamellae with offsets of up to 20 μm (Figure 4b). Along the through-going shear-fractures the grain size is significantly reduced and fault gouge is present (Figure 4c). Electron probe analyses (EMPA) show that the small gouge fragments maintain the original chemical composition of the surrounding orthoclase matrix and/or the albitic lamellae. Even narrow albite lamellae show well-defined boundaries (Figure 4b). White mica does not show any signs of decomposition, even in densely cracked regions. Samples deformed at 0.75 and 1.0 GPa do not show systematic microstructural differences except for a higher density of cracks in the sample deformed at higher confining pressure.

3.3.2. Samples Deformed at 900°C

3.3.2.1. Fracturing

Shear fractures oriented at 30–60° to the compression direction are pervasive in all samples (Figure 5). In low-strain samples the shear cracks form short (from tens of microns to ~1 mm length) parallel sets. They are concentrated in the most strongly deformed parts of the samples (Figure 5a), which correspond to the highest-temperature regions (marked by the thermocouple positions in the figures). In higher-strain samples
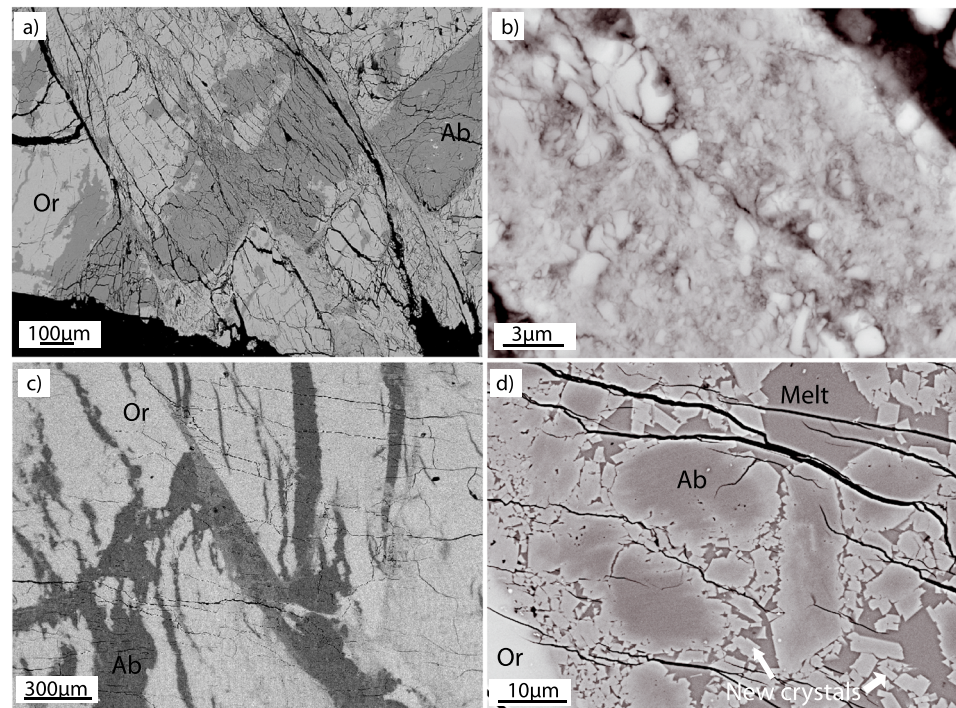
Figure 6. SEM backscatter images (BSE) of cracks and related microstructures in pink and white K-feldspar samples, both deformed as is. Compression direction is vertical in all images. (a) Formation of parallel shear cracks in the lower part of sample 250 (900°C, 1.5 GPa). Differential movement of the fractures is evident from the offset of the albite lamellae. Formation of fine-grained gouge often occurs along the main fractures. (b) Detail of Figure 6a. Fine-grained crushed fragments in through-going fractures. Angular fragments have a size of ≪ 1 to 3 μm. Neither melting nor compositional changes are observed. (c) Gouge formed along a shear fracture in the central part of the sample 222 (900°C, 1.0 GPa). Note the chemically homogenized composition of the fine-grained gouge. (d) Detailed picture of Figure 6c. The small gouge fragments show a chemically homogenized composition. On the contrary the core of the larger (20–50 μm) fragments maintain the same composition as the starting material. Melt is present in between the gouge fragments.

(Figure 5b) the shear fractures are longer and form conjugate sets. Displacement along the shear fractures is evident from the offset of albite lamellae or twins and varies from a few micrometers in low-strain samples to 100–150 μm in high-strain samples.

High-strain samples may develop brittle through-going shear zones at an angle of 40–60° to σ_1 (Figure 5b). The shear zones are surrounded by a large number of smaller, subparallel microfractures whose density generally increases toward the shear zones. The presence of microfractures around the main shear zones causes the undulatory extinction of such regions with respect to the intact crystal, as observed by *Tullis and Yund* [1977, 1987]. Locally, especially along the through-going shear zones or along major conjugate fractures, fault gouge is found (Figures 6a and 6c). There are two different types of gouge: (a) gouge without melt (Figures 6a and 6b) and (b) gouge containing interstitial melt (Figures 6c and 6d).

(a) Fault gouge formed in the outer parts of the samples (near the pistons, where temperatures are lower) consist of angular fragments with sizes ranging from submicron (<100 nm) to ~20 μm (Figures 6a and 6b). The crushed fragments form thin layers (< 250 μm) of gouge (Figure 6b) that maintain their original chemical compositions, and there is no evidence of melt formation.

(b) Fault gouge-containing melt (Figures 6c and 6d) occurs in the central parts of the samples. The gouge consists of a few larger fragments surrounded by a fine-grained and chemically homogenized matrix (individual fragments cannot be resolved at a magnification up to 17,000X). The few larger (20–70 μm) fragments show no chemical homogenization in their cores, surrounded by chemically homogenized rims. The rims most likely formed by crystallization of new grains on the original clast surfaces as demonstrated by the well-developed crystal faces observed in some rims (Figures 6d and 7c). Melt is present in small domains randomly distributed in the homogenized material (Figure 7).
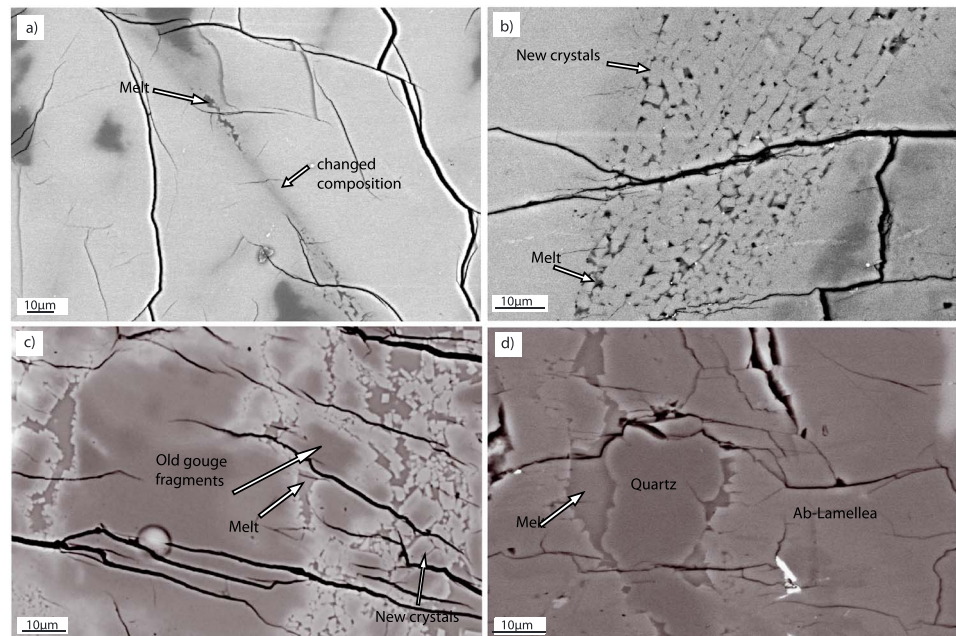
Figure 7. SEM backscatter micrographs of microstructures involving melting in experiments at 0.75, 1.0, and 1.5 GPa, 900°C. Compression direction is vertical in all images. (a) Formation of isolated melt pockets, containing euhedral new crystals, along a shear fracture in sample 258. The crack is visible as a chemically homogenized region. The elongated melt domains are orientated at ~40° to the compression direction. (b) Formation of oriented euhedral crystals with homogeneous composition along a shear fracture in sample 276. The crystals are oriented in the direction of shear. Residual melt occurs in interstitial spaces. (c) Melt pockets distributed in a gouge (sample 222). The chemically unchanged cores of the larger fragments are overgrown by chemically homogenized rims, whereas the small grains have a completely homogenized composition. (d) Melt formed around a small quartz grain contained in an albite lamella in sample 223. The melt is distributed along grain boundaries oriented parallel to the compression direction. The quartz grain shows rounded edges indicating partial melting.
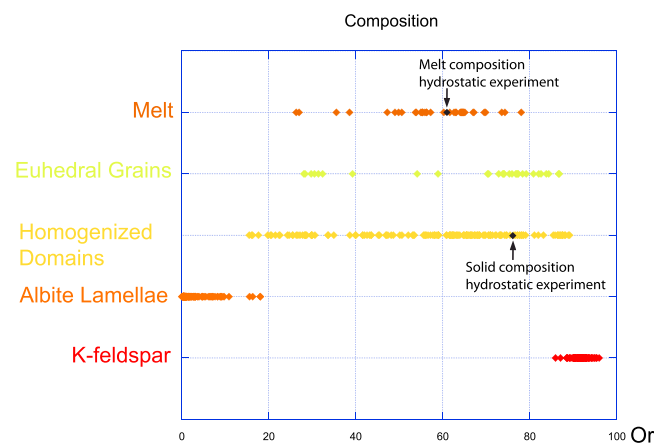

Figure 8. Chemical compositions of albite lamellae, K-feldspar matrix, chemically homogenized domains, melt, and new euhedral grains. The compositions of albite lamellae and K-feldspar are fairly consistent, but the chemically homogenized domains and melt show a wide range of compositions suggesting that they are derived from mixing between the K-feldspar and the albite lamellae. The newly formed euhedral crystals show, for the most part, two distinct compositions of ~ $Ab_{70}Or_{30}$ and ~ $Ab_{20}Or_{80}$. The compositions of the melt and homogenized fragments in the hydrostatic powder experiment are marked in black.

3.3.2.2. Partial Melting

Partial melting in the perthite single crystals is almost always spatially associated with brittle deformation (examples of melt without brittle deformation are rare small quartz inclusions with a small melt halo), occurring along shear cracks and through-going fractures containing fine-grained gouge (Figures 6c, 6d, and 7a–7c). The melt, which is clearly recognized in SEM backscatter images by its darker contrast (Figure 7), contains randomly distributed spherical bubbles with a diameter of 2–4 μm (Figure 7b), and a higher density of unloading cracks (approximately normal to the compression direction, Figures 6d and 7c), as a result of localized regions of greater permanent deformation becoming extended during later elastic unloading of the whole sample.
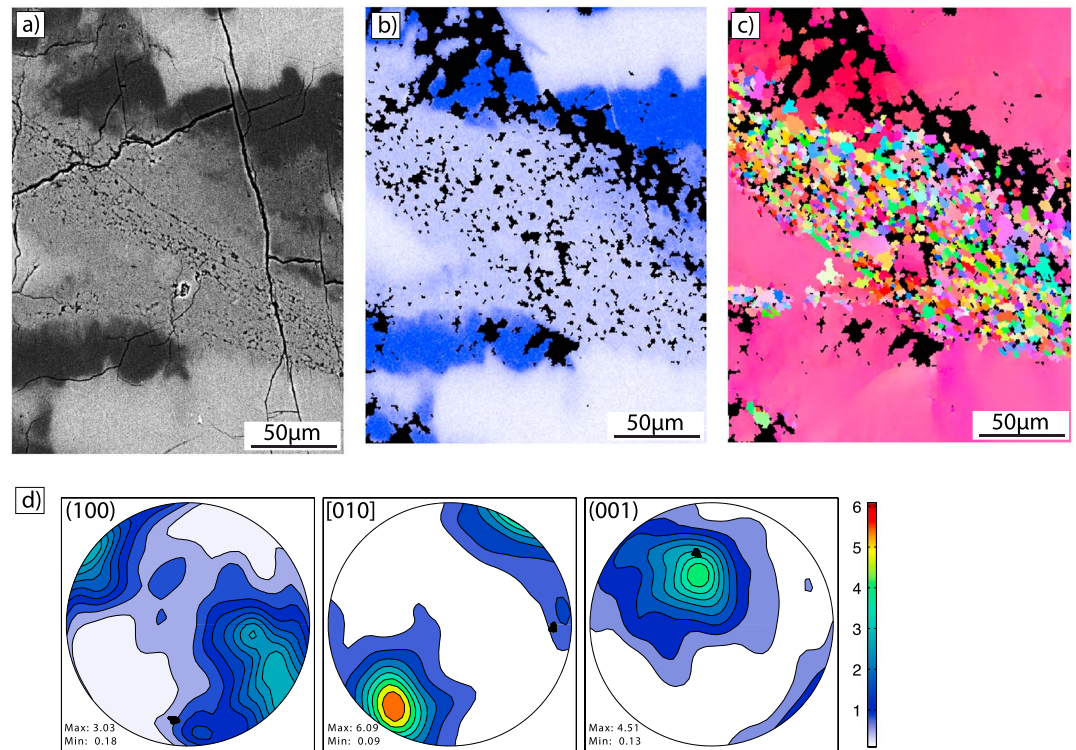
Figure 9. Crystallographic preferred orientation (CPO) measured with EBSD of a chemically homogenized region containing melt and newly formed euhedral crystals. The compression direction is horizontal in all figures. (a) SEM backscatter image of the analyzed region. Albite lamellae (dark gray), Or-rich matrix (light grey), and chemical homogenization (intermediate grey in the center of image) are easily distinguishable. (b) Na element distribution map. (c) Processed orientation maps of the homogenized region. (d) Pole figures of the chemically homogenized domain showing a strong CPO. The contours refer to the polycrystalline material, and the black points refer to the orientation of the single crystal. The orientation distribution function for the polycrystalline feldspar aggregate was calculated considering a half width of 10° using the MTEX toolbox for (Matlab) [*Hielscher and Schaeben*, 2008].

The melt is typically distributed interstitially between large clasts and gouge particles, but it may also coalesce to form melt domains of different size and irregular shape (Figure 7c). Locally, elongation of melt domains occurs along the shear fractures (Figure 7a). Often the melt domains contain densely packed, small (up to 20 μm), newly formed euhedral crystals (Figures 7b and 7c) with a chemical composition intermediate between the original K-feldspar matrix and the albite lamellae (Figure 8).

Melt domains in the fine-grained gouge (Figure 7c) are generally larger (diameter up to 20 μm) than the elongated melt regions along the shear fractures (Figure 7a) and typically contain newly formed crystals. The new grains either nucleate on gouge fragments forming irregular rims or occur as new euhedral grains with straight boundaries, sometimes randomly distributed in the melt domains (Figure 7c). All new grains have a chemical composition different from that of the starting material. The composition may vary but is intermediate between the Or-rich matrix and the albite lamellae (Figure 8). Below, this intermediate composition is referred to as "chemically homogenized."

Melt also forms around small quartz grains contained in the albite lamellae (Figure 7d). In this case the melt is present as a thin film (up to 10 μm thick) along grain boundaries. The relict quartz crystals show smooth, lobate boundaries resulting from the partial melting process.

The chemical composition of the melt is inhomogeneous and varies from ~ $Ab_{70}Or_{30}$ to ~ $Ab_{80}Or_{20}$ (Figure 8) depending on the amount of material that has melted and the local composition (local volume ratio of Albite and K-feldspar). Melt formed in the K-feldspar-rich regions of the perthite shows Or-rich compositions whereas melt formed close to albite lamellae shows more albitic compositions, so that the melt composition may vary within a single melt domain.
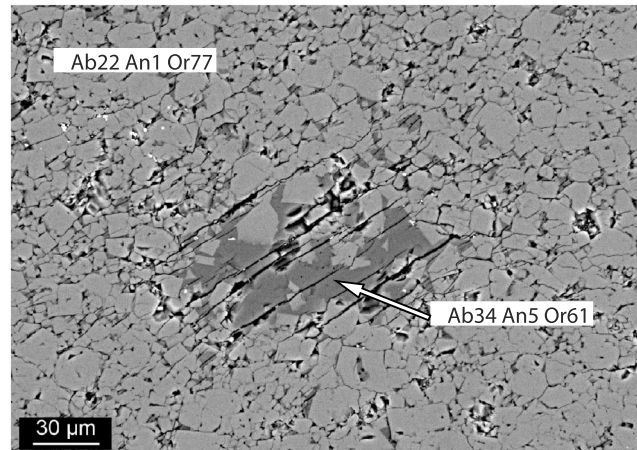
Figure 10. SEM backscatter image of a powder sample (267) hydrostatically hot pressed at 900°C and 1.0 GPa for 34 h. The original powder material was composed of albite and K-feldspar fragments. After hot pressing, the material shows a completely homogenized chemical composition of $Ab_{22}An_1Or_{77}$ and formation of melt with a composition of $Ab_{34}An_5Or_{61}$. Most of the melt is collected in large melt pockets randomly distributed in the sample.

EBSD analysis (Figure 9) of zones containing melt and newly formed euhedral crystals shows that the crystals have a well-defined and strong crystallographic preferred orientation (CPO). In the pole figures (Figure 9d), the orientation of the euhedral crystals shows a strong alignment of their (010) planes subparallel to the orientation of the shear plane, while the poles of (100) are parallel to the inferred shear direction of the fractures.

White mica, where present along the {110} cleavage planes (Figure 1), is usually preserved in the undeformed and/or colder parts of the samples (e.g., sample ends close to pistons). In the regions of melt formation (corresponding to the more cracked and deformed regions of the samples), there is either no white mica or it is replaced by fine-grained aggregates that have a dark brown color under the light microscope.

3.3.2.3. Melt Content and Composition

To determine the total melt fraction of the Kfsp-Ab-H_2O system, a hydrostatic experiment was performed on pink K-feldspar powder (grain-size of 12–20 µm) at 900°C and 1.0 GPa for 42 h (Figure 10). The powder was placed between alumina pistons cut at 45° to the compression direction but was not deformed. In the
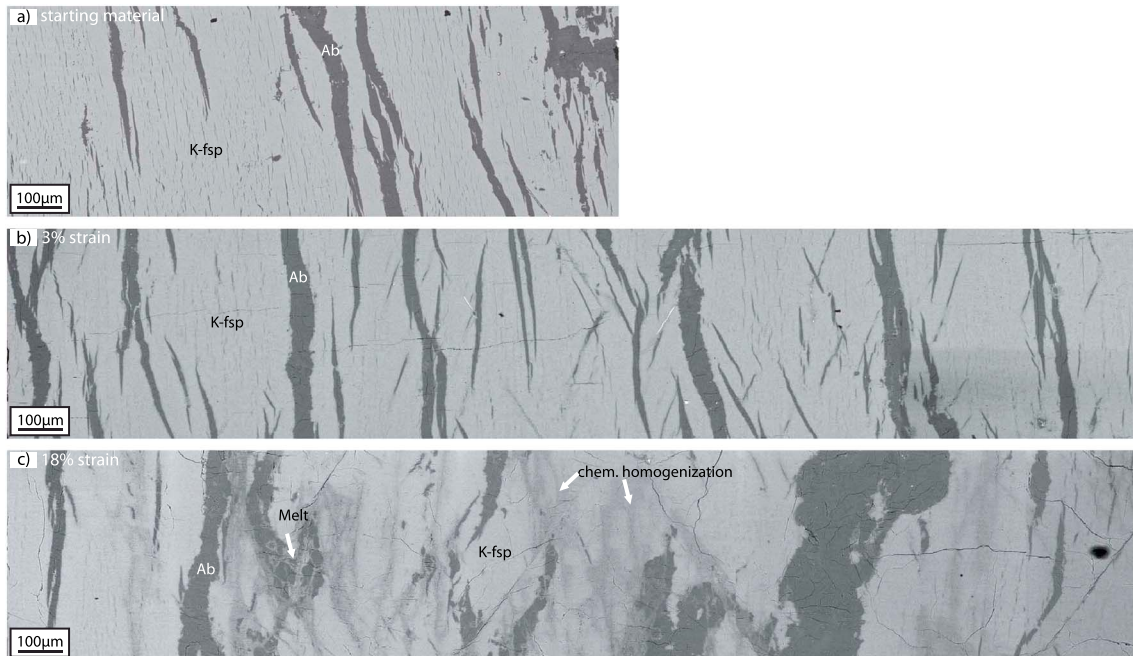
Figure 11. SEM backscatter images showing the relationship between microstructure, melt formation, and strain. (a) Pink K-feldspar starting material. (b) Microstructure of axial compression experiment stopped at peak strength (294, 900°C, 0.75 GPa, 3% strain). A few cracks are present in the central part of the sample, where little homogenization occurred. No melt was detected at this strain. (c) Microstructure of axial compression experiment (295) at 900°C, 0.75 GPa, and 18% strain. The sample shows pervasive fracturing and related chemical homogenization. Melt pockets are present in homogenized regions and along shear cracks.
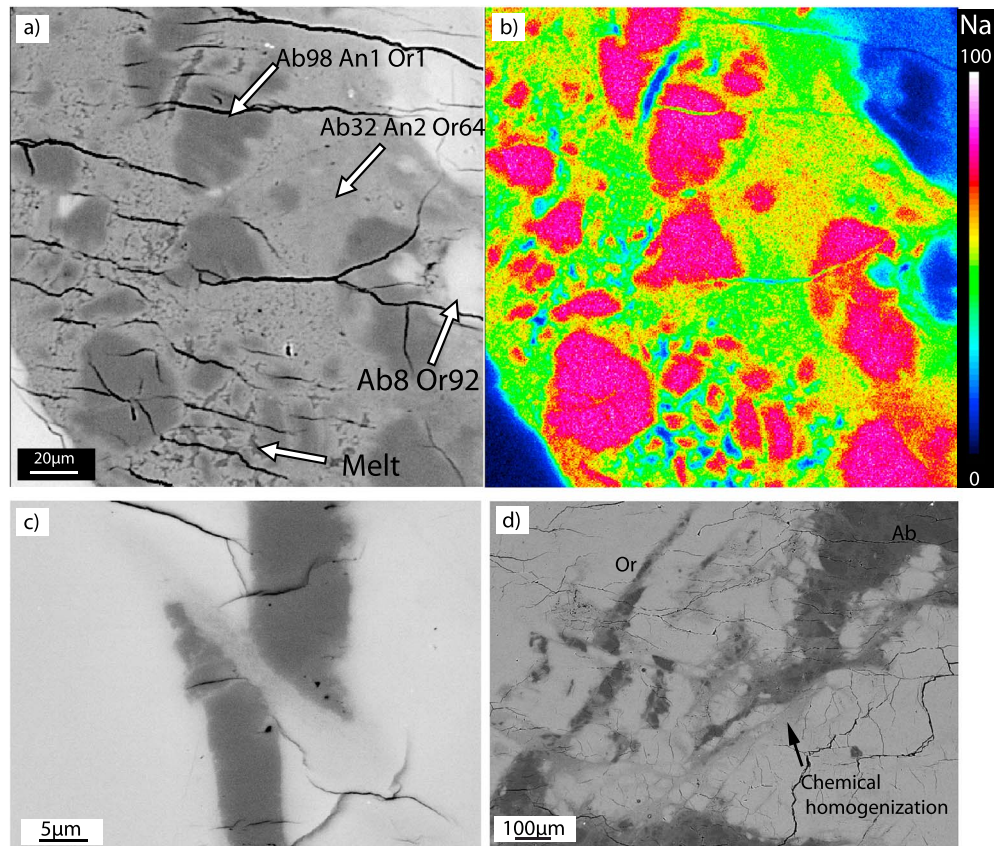
Figure 12. Chemical analysis of a gouge formed in high strain samples. (a) Backscatter electron image of sample 222 (900°C, 1.0 GPa). Note that chemical homogenization ($Ab_{32}An_{02}Or_{64}$) occurs in the fine-grained matrix, whereas the larger fragments maintain the original albitic composition of $Ab_{98}An_{01}Or_{01}$. The surrounding intact material is Orthoclase ($Ab_{08}Or_{92}$). (b) The EPMA element distribution map of Na shows inhomogeneous composition of the chemically homogenized matrix, which is represented in the yellow-greenish color. The small blue regions in the middle of the gouge represent melt pockets. The albitic fragments with a high Na content are shown in pink. (c) Sample 216 (900°C, 1.0 GPa). Shear fractures oriented at 50° to the compression direction are detectable only due to the displaced albite lamellae and the formation of 20 µm wide zones of chemically homogenization along the cracked region. In the chemically homogenized zone no particles are distinguishable by means of SEM. (d) Sample 216 (900°C, 1.0 GPa). Zones of chemically homogenized composition overgrowth and seal microfractures.

hydrostatic powder experiment (Figure 10) most of the melt has collected in a thin band between the layer of powder and the top piston interface, indicating a relatively low viscosity and high mobility of the melt. The composition of the melt is homogeneous ($Ab_{34}An_{05}Or_{61}$). Some smaller melt domains are randomly distributed in the solid powder phase, which has a uniform composition of $Ab_{22}An_{01}Or_{77}$ (Figure 10).

The melt fraction was determined by calculating its area fraction on SEM backscatter images. At 900°C the fine-grained powder produces a melt fraction of $\Phi_{vol} = 0.05$ to 0.06. This represents an upper limit because some pores and plucked grains contribute to the SEM estimate of the melt fraction (Figure 10). The H_2O content of the melt is ~10 wt %, determined by taking the difference between the average total of the EMPA analyses and the theoretical total of 100%. This value may have an error of at least ± 1 wt % given the problems of determining the H_2O contents of melts [*Johannes and Holtz*, 1996]. The H_2O content of the melt was only determined in the powder sample, because most melt domains in the deformed samples were too small to be measured.

In the deformed single-crystal experiments the estimation of the melt fraction was difficult due to the low and variable melt percentage, and because the melt was well dispersed between the fine-grained gouge fragments formed along the shear fractures. However, we observed in samples deformed at 900°C and 0.75 GPa a general increase of melt fraction with increasing strain (Figure 11): the strongly deformed sample
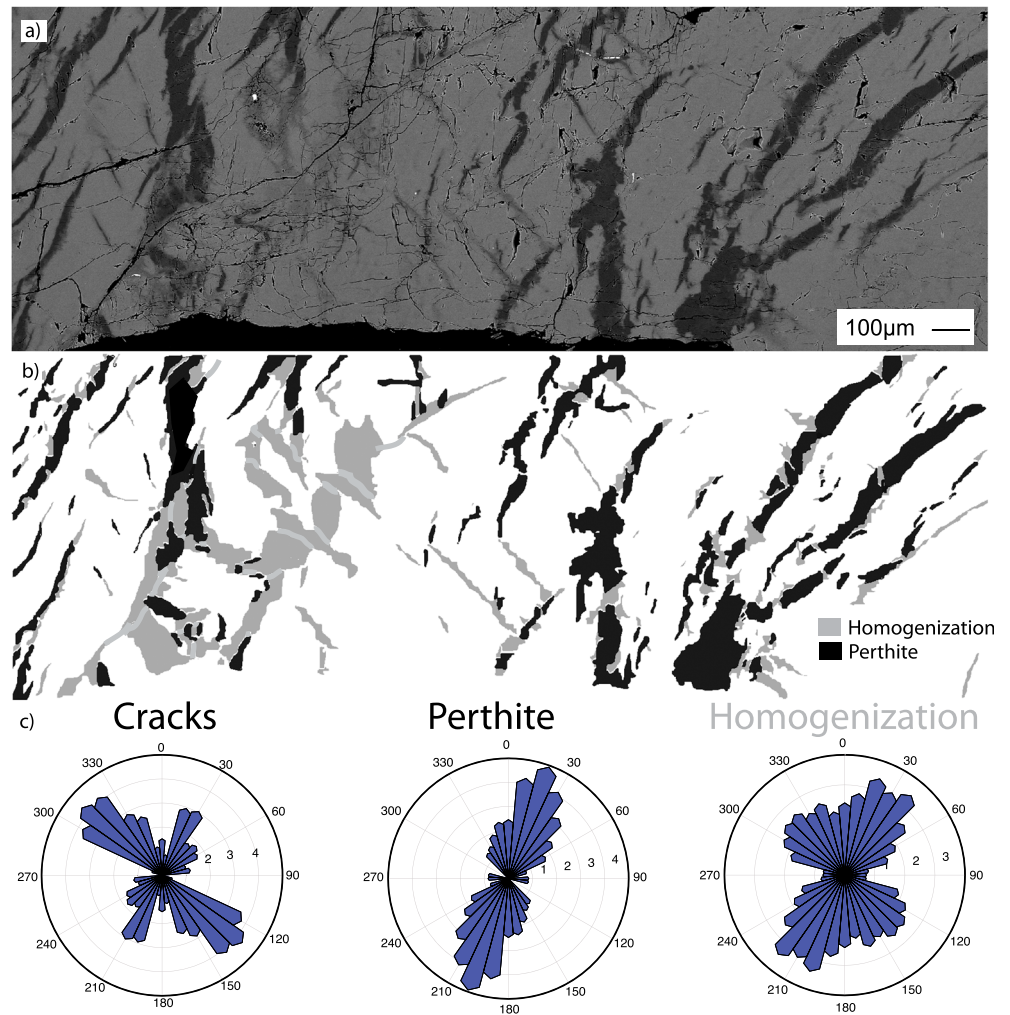
Figure 13. Relationship between cracks and chemical homogenization in sample 250 deformed at 900°C, 1.5 GPa. Compression direction vertical. (a) SEM backscatter image. Three phases are visible: K-feldspar matrix (light grey), albitic lamellae (dark grey), and chemically homogenized region (intermediate grey). (b) Grey level slicing of the BSEM images created with Image SXM showing the distribution of the albitic lamellae and the chemically homogenized regions. (c) Rose diagram showing the orientation relationship between cracks, albitic lamellae, and homogenize zone with respect to the compression direction (vertical).

(18% strain) contains a considerably larger amount of melt than the low-strain experiment (3% strain) in which almost no melt was detected. Conversely, in samples deformed at 900°C and 1.5 GPa the melt fraction did not depend on strain. After only 3% strain (where the stress is ~300 MPa, 10% below maximum peak values) the sample contained almost the same amount of melt as in the high strain samples.

3.3.2.4. Chemical Homogenization of Solid Material

Deformed samples contain chemically homogenized zones, exclusively in fractured regions (Figures 6c and 12). The composition of these zones varies from $Ab_{10}Or_{90}$ to $Ab_{83}Or_{17}$ (Figure 8) and suggests that the compositional changes arise from differential mixing of the Or-rich matrix ($Ab_{08}An_0Or_{92}$) with the albite lamellae ($Ab_{98}An_{01}Or_{01}$) present in the starting material (Figure 8).

Chemically homogenized zones are found either in gouges formed along shear fractures (where the fragmented material has an intermediate chemical composition of $Ab_{32}An_{02}Or_{64}$, Figures 12a and 12b), as roughly symmetric bands (up to 90 μm wide) surrounding fractures (Figure 12c) and locally as overgrowths sealing old fractures (Figure 12d). Chemical distribution maps (Figure 12b), EPMA measurements, and BSE images show well-defined transitions (over less than 5 μm distance) between the chemically
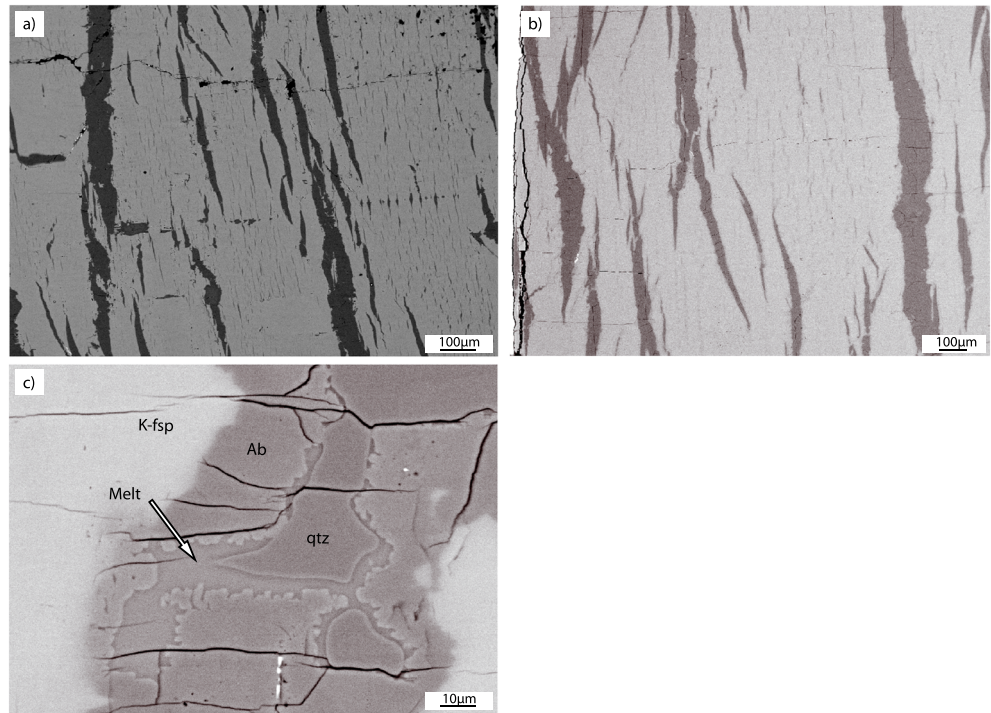
Figure 14. SEM backscatter image (BSE) showing the microstructure of the hydrostatic experiment (sample 271) kept at 900°C and 1.0 GPa for 71 h. (a) Backscatter image of the starting material (pink K-feldspar). (b) Microstructure of the hydrostatic experiment. Comparison between starting material Figure 14a and hydrostatic experiment 14b shows no substantial changes. Albitic lamellae and matrix do not show any chemical homogenization and no shear cracks were formed. (c) Melt formation in the hydrostatic experiment was observed only around quartz grains present in the albitic lamellae. The melt film forms a homogeneous rim all around the quartz crystal.

homogenized regions and the surrounding undisturbed K-feldspar starting material. As visible in Figure 13 the orientation of the zones of compositional change broadly corresponds to the orientation of the conjugate fractures, confirming the close link between cracking and chemical homogenization.

It should be noted that it is impossible to distinguish in SEM images the individual fragments of the chemically homogenized material (Figures 12 and 7a). This is different from nonhomogenized and melt-free gouge, where even submicron-sized fragments are clearly identified (Figure 6b). In order to characterize the chemically homogenized regions, we attempted EBSD measurements in such regions. It was possible to acquire and index individual EBSD patterns, indicating the crystalline nature of the material. However, it was not possible to identify regions with the same orientation larger than a few points (at a step size of 1 μm), so it is likely that these zones consist of extremely fine grained material with a grain size that cannot be resolved at this EBSD step size.

3.3.3. Hydrostatically Heat-Treated Sample

Hydrostatic experiments (Figure 14) were performed in order to distinguish between microstructures formed during pressurization and heating from those produced by deformation. In hydrostatic experiments, cracking is rare and only present at the end regions of the sample where it contacts the pistons, producing small axial fractures with no displacement. A few isolated fractures are found close to mica grains. These fractures are oriented at ~35° to the {100} direction, corresponding to the orientation of the mica flakes in the starting material.

Compositional changes are almost absent in comparison to deformed samples. Some chemical homogenization seams are present along fractures in the vicinity of mica, but no homogenization occurs between albite and K-feldspar. Even the thinnest albite lamellae (1–10 μm) are undisturbed and maintain the same appearance and characteristics as the lamellae in the starting material (Figures 14a and 14b). Melt is present only as thin films around quartz inclusions in some albite lamellae (Figure 14c).

4. Discussion

Fracturing and melt formation are strongly connected in all samples deformed above 700°C. Thus, the discussion will focus on two main aspects: (1) the relationships between fracturing and melt formation and (2) deformation mechanisms within fractured zones in the presence of melt.

4.1. Fracturing and Melt Formation

4.1.1. Fracture Microstructures

The shear fractures in 700° and 900°C experiments form angles of 30° to 60° with respect to σ_1. For the high confining pressures used in these experiments, typical shear fractures of 45° to σ_1 would be expected for a Coulomb-Mohr failure criterion. The fracture planes are normal to the {001} plane and intersect the {001} and {010} planes at ~45° (Figures 4 and 5). From this geometry, it can be concluded that the shear fractures are at least in part crystallographically controlled. The {110} and {1–10} planes are perfect cleavages in feldspars and have the correct orientation for the conjugate fracture systems. In addition, cleavage fractures explain the partly asymmetric orientation of the conjugate fracture system with respect to σ_1 (Figure 5) and fracture angles larger than 45° to σ_1. The importance of cleavage systems for feldspar deformation has already been pointed out by *Tullis and Yund* [1987, 1992].

Furthermore, white mica can locally be present along some cleavage planes (Figure 1) and will weaken such planes. The role of white mica in melt formation along cracks will be discussed below.

The stress-strain curves for K-feldspar samples deformed at 700°C show features typical of brittle deformation: peak strength is slightly higher than the confining pressure, and there is a positive dependence of peak stress on confining pressure. The strength at 700°C and 1 GPa confining pressure is similar to that of polycrystalline anorthosite samples (deformed at higher strain rates of $10^{-5}\,s^{-1}$ [*Hadizadeh and Tullis*, 1992] and at the same strain rates [*Tullis and Yund*, 1992]), indicating that K-feldspar has a similar strength as plagioclase. Brittle deformation as the dominant deformation mechanism at 700°C is supported by microstructural observations, which show extensive cracking in the samples, intensive grain size reduction in fault gouges, and the complete absence of melt (the latter is consistent with the range of solidus temperatures for feldspar melts at low H_2O contents) [*Holtz et al.*, 1992; *Johannes and Holtz*, 1996].

At 900°C deformation of perthite single crystals also occurs along brittle structures such as shear cracks and conjugate fracture arrays. At 900°C, however, there is melt formation associated with the cracking. The melt in our experimentally deformed K-feldspars is always found in connection with brittle deformation, whereas intact material (represented by the hydrostatic experiments), on the contrary, does not melt at 900°C (even though this temperature is 200°C above the solidus). These observations suggest that melting of feldspar above the solidus is promoted by deformation and fracturing.

Three lines of evidence suggest that the brittle structures formed during deformation do not control the rheology of the samples: (i) The differential stresses (Figure 3) are far below the Goetze criterion [*Kohlstedt et al.*, 1995] ($\sigma_1 - \sigma_3 \leq Pc$). (ii) The friction coefficient would be very low ($\mu \sim 0.1$ to 0.2 for experiments at Pc of 1.5 GPa and 1.0 GPa) instead of ~0.6 for silicates on fractures oriented at 45–50° to the compression direction, and (iii) the stress-strain curves show an inverse dependence of peak strength with increasing confining pressure (flow stress at 1.5 GPa is 330 MPa, at 1.0 GPa is 400–480 MPa and at 0.75 GPa is 680 MPa; Figure 3c). In addition, the fracture density is higher in the higher-temperature regions of the crystals (Figure 5) so that the brittle features are, at least in part, thermally or melt activated. The observed temperature effect is likely due to interaction of cracking with the melting process. All of these observations indicate that rheology is not entirely friction controlled but is considered to be semibrittle with a viscous component.

4.1.2. Melt Formation and H_2O Content

The amount of H_2O measured (~10 wt %) in the quartz-free feldspathic melt of the powder experiment is lower than the data compilation of *Johannes and Holtz* [1996] for a water saturated granitic melt at Pc = 1 GPa. Data for feldspathic melt (which has a higher H_2O solubility than quartz-bearing melt) [*Johannes and Holtz*, 1996] at 1 GPa are not available, but *Behrens et al.* [2001] obtained values of ~15 wt % H_2O at 800 MPa in albite melt. Between 200 MPa and 500 MPa the H_2O solubility in feldspathic melts follows almost a linear trend [*Behrens*, 1995] so that at a pressure of 1 GPa the H_2O solubility in an Or-Ab-melt is expected to be greater than 15 wt % [*Behrens*, 1995; *Behrens et al.*, 2001]. Thus, the measured H_2O content in our powder experiment (~10 wt %) indicates an H_2O-undersaturated melt, even if a measurement error of 10–20% is considered.

The melt fraction calculated by thermodynamic modeling for an H_2O content of 0.3 wt % is ~ 5 vol % (4.8 wt %) (Figure 2). Using the measured H_2O content of ~10 wt % in the melt and an H_2O content of the sample of ~0.3 wt %, the expected melt fraction should be ~3 wt %. The estimated melt fraction in the powder experiment is 5 to 6 vol % as an upper limit. Considering the errors in the thermodynamic modeling, the SEM melt fraction estimates and the extrapolation of volume fraction (3-D) from 2-D observations (SEM and thin section), the results indicate melt fractions in the powder experiment of ~3–5 wt %. In the deformed single crystals, the melt fractions are considerably smaller (because of the lower H_2O content of ~0.1 wt %) but impossible to quantify. Equilibrium is more difficult to attain in the deformed single crystals than in powder samples, and given the fact that the melt in the powder experiment is H_2O undersaturated, it is even more likely that the melts in the deformed crystals are H_2O undersaturated.

4.1.3. Relationship Between Deformation and Melting

At 900°C (1.0 GPa), ~ 200°C above the solidus temperature, melting is expected and is confirmed by the presence of melt in deformed samples. However, in the hydrostatically heated single crystal (900°C at 1.0 GPa), no melt was detected.

As melting is a surface process, the melt always forms at grain boundaries [e.g., *Hess*, 1994; *Greenwood and Hess*, 1998]. For H_2O-undersaturated melts the solidus curve has a positive Clausius-Clapeyron slope. At the solidus P-T conditions, melt formation will increase the local pressure due to a volume increase and will shift the system into the subsolidus region. Thus, any melting progress in such a system is dependent on a volume increase by, e.g., dilatancy. This effect is demonstrated by the powder experiment, where sufficient porosity exists and the melt fraction has increased to roughly the maximum melt fraction attainable at the given P-T conditions in the presence of small amounts of H_2O (in addition, the very fine grain size of the powder and the mixing produce a larger contact area of albite and K-feldspar and help to obtain uniform equilibrium melt and solid compositions).

Variations of melt content in deformed and undeformed samples have already been reported by *van der Molen and Paterson* [1979], *Misra et al.* [2009], and *Tumarkina et al.* [2011]. *Misra et al.* [2009] observed an increase of melt fraction (of 1.72 times) in deformed samples compared to undeformed samples of mica. *Tumarkina et al.* [2011] analyzed the possible energy contributions of deformation to the melting process. The effect of deformation on solid-state chemical reactions has been studied by *De Ronde et al.* [2004, 2005] and has been attributed to an increase in defect energy and the creation of new reaction surfaces [*De Ronde and Stünitz*, 2007]. *Tumarkina et al.* [2011] conclude that an increase in surface and defect energy does not contribute sufficiently to the activation energy for melting. The contribution of defect and surface energy in the deformed feldspars of this study is somewhat higher than that of the viscously deformed micas of *Tumarkina et al.* [2011], but it is still 1 or 2 orders of magnitude too small to cause the difference in melting rate between deformed and undeformed samples. We concur with *Tumarkina et al.* [2011] that the larger melt fraction in deformed samples is caused by dilation effects during deformation. In the case of mica deformation [*Tumarkina et al.*, 2011], melting is promoted by a reduction in the effective viscosity during macroscopic shear deformation of the rock. The viscous deformation eliminates grain-scale mean stress perturbations caused by the volume change of the melting reaction and leads to more uniform melting resulting in an increased melt fraction. In the case of feldspar melting in this study, the positive feedback between deformation and melting is most likely caused by the dilatancy during cracking. Thus, from the observations and the inferred melt reactions, it can be concluded that melting in the deformed samples is facilitated by dilatancy from the cracking process, whereas it is suppressed by the lack of dilatancy in the hydrostatically heated sample.

In the case of nonhydrostatic stress states, the pressure is given by the mean stress, which is higher than $P = \sigma_3$. An additional contribution of deviatoric stress is expected to increase the effect of melt suppression for the positive Clapeyron slope of the melting curve. However, for grain boundaries at a small angle to σ_1 the effect may be considerably lower than for boundaries at a large angle to σ_1. This situation may play a role in the anisotropic melt distribution observed in the nonhydrostatic stress experiments. Thus, the accumulation of melt in relatively low-pressure sites [e.g., *Stevenson*, 1989] may be partly caused by anisotropic melt formation in addition to melt migration processes.

4.2. Viscous Deformation of Samples in the Presence of Melt

As discussed above, deformation of feldspars in these experiments at high pressures and temperatures occurs initially by brittle processes. However, the relatively low flow stresses, the presence of melt as well as

chemically homogenized zones, and the formation and growth of new crystals within and around melt domains indicate that viscous creep processes dominate the deformation.

Not many deformation experiments have been carried out on K-feldspar [*Willaime and Gandais*, 1972; *Willaime et al.*, 1973, 1979], and description of naturally deformed K-feldspars are also not frequent [*Debat et al.*, 1978; *Sacerdoti et al.*, 1980; *Vidal et al.*, 1980; *White and Mawer*, 1988; *Bell and Johnson*, 1989; *Menegon et al.*, 2008]. So far, no systematic differences between K-feldspar and plagioclase in terms of crystal plastic deformation have been detected (for reviews see *Tullis* [1983, 2002] and *Fitz Gerald and Stünitz* [1993]) so that a comparison of K-feldspar with plagioclase (for which there are far more data and observations) is used here for the interpretation of our results.

Tullis and Yund [1992] conclude from deformation experiments performed on anorthosite that plagioclase starts to deform by dislocation creep at 900°C and 1.0 GPa (although hydration reactions and cracking occur). Single crystals of plagioclase deformed at 900°C and 1 GPa in the same orientation show similar or higher flow stresses compared to the K-feldspars of this study [*Stünitz et al.*, 2003]. The plagioclase single crystals deformed by dislocation glide and some cracking, while recrystallization occurred by growth of small, defect-free clasts. Conversely, in our perthite crystals there is no microstructural evidence for dislocation glide or dynamic recrystallization. One of the reasons for this situation is that two of the main slip systems ((010) and (001) slip planes) are not in an orientation for easy slip, and only the (110) ½ [−112] and (1−11) ½ [110] slip systems could be activated, but these are not easy slip systems in K-feldspar [*Sacerdoti et al.*, 1980]. Another possible explanation for the apparent absence of dislocation-related deformation features may be the intense twinning of the microcline matrix and the ubiquitous albite exsolution lamellae at all scales. Both sets of these planar defects will effectively impede the movement of dislocations.

4.2.1. Diffusion Creep

In the absence of crystal plasticity, the viscous component of semibrittle deformation is likely to be diffusion creep and grain boundary sliding (dissolution-precipitation creep). Microstructural observations are consistent with such an interpretation:

The K-feldspar samples deformed here contain widespread evidence for melting and chemical homogenization in cataclastic regions. Chemically homogenized regions occur in and around fractures containing melt (Figures 11 and 13). Chemical homogenization is also evident in the fine-grained gouge fragments, which cannot be distinguished and resolved in SEM backscatter images (Figures 6 and 7) or from EBSD analyses (Figure 9). The effect is extensive in the powder experiment where the entire material shows a homogeneous intermediate composition ($Ab_{22}An_{01}Or_{77}$). The compositional homogenization indicates extensive ionic exchange between albite and K-feldspar grains and melt.

The distinction between volume and grain boundary diffusional exchange of K and Na ions to produce chemically homogenous regions is not easy to make in these samples. Diffusion data by *Brady and Yund* [1983] and *Christoffersen et al.* [1983] on interdiffusion of K and Na in alkali feldspars by volume diffusion (see also review in *Yund* [1983]) indicate that diffusional exchange at an interdiffusion coefficient ($D^−$) of $10^{−12}$ to $10^{−13}$ cm^2/s would produce K-feldspar-rich rims on albite or albite-rich rims on K-feldspar of 0.5 to 5 μm in 3 days (the duration of higher-strain deformation experiments reported here). In some of the clasts found here, K-feldspar-rich rims of 1 to 10 μm are formed (Figures 6d, 7c, 12a, and 12b). These rims have formed in the presence of melt, and given the presence of well-defined crystal faces it is concluded that the compositional change is due to overgrowth of a homogeneous feldspar in equilibrium with the melt, and not a volume diffusion exchange. In the cataclastic regions the homogenized rims can be much wider (up to 90 μm) and are also found in contact with melt (Figures 6c and 6d). The clast size in such regions can be much smaller than 1 μm (Figure 6d) so that volume diffusion exchange could produce the chemical homogenization during the experiment. Alternatively, replacement by solution-precipitation during the melt-forming reaction is a feasible mechanism to produce the chemically homogeneous regions.

One observation suggests that volume diffusion does not always operate in these samples: even the very thin stringlet-type albite lamellae (1 μm width) remain intact in the hydrostatically heated sample (Figure 14), in larger clasts after deformation (Figures 12a and 12b), or with minor chemical homogenization along their boundaries (Figure 7b). Thus, replacement and dissolution-precipitation processes appear to dominate over volume diffusion in producing chemically homogeneous feldspar.

For replacement and dissolution-precipitation, the presence of melt enhances these processes by increasing the transport rate along grain edges or grain boundaries [*Raj*, 1982; *Pharr and Ashby*, 1983; *Cooper and Kohlstedt*, 1984b; *Cooper et al.*, 1989; *Kohlstedt*, 1992; *Kohlstedt and Zimmerman*, 1996; *Tullis and Yund*, 1996; *Hirth and Kohlstedt*, 2003]. The deformation of olivine by diffusion creep takes place at higher strain rates in the presence of melt [e.g., *Hirth and Kohlstedt*, 1995b], and a major increase in strain rate is found above melt fractions of 0.07 [*Hirth and Kohlstedt*, 1995b]. The strain rate increase is dependent on the wetting of grain boundaries [*Hirth and Kohlstedt*, 1995b; *Dimanov et al.*, 2000], which, apart from the melt fraction, is also dependent on melt viscosity [*Cooper and Kohlstedt*, 1984a, 1984b]. In the powder experiment, many of the grain boundaries are wetted with melt (Figure 10) at a melt fraction of ~5%. At the lower melt fractions found in the deformed samples, melt is also observed along grain boundaries (Figure 7b).

Tullis and Yund [1991] have observed diffusion creep in fine-grained albite aggregates at 900°C, $10^{-6}\,s^{-1}$ strain rates when the H_2O content is high enough (0.9 wt %) and conclude that a direct transition from cataclastic deformation to diffusion creep is likely under such conditions. The melt can substitute the high H_2O contents in the case of our feldspar experiments, as has been demonstrated by *Dell'Angelo et al.* [1987] in feldspar-bearing aggregates. The melt threshold for diffusion creep deformation is 3–5% in their experiments —very similar to the melt percentages in our single crystal experiments. *Dimanov et al.* [1998, 2000] have deformed plagioclase grains of 12 to 16 μm in size in the diffusion creep regime in the presence of melt. However, temperatures were considerably higher (1100 to 1350°C) than in the perthite experiments here. The melt films are found along grain edges in the lower temperature hot pressing experiments [*Dimanov et al.*, 1998], whereas in higher temperature hot pressing, they may wet the grain boundaries [*Dimanov et al.*, 2000].

In addition, *Sundberg and Cooper* [2008] deformed orthopyroxene and olivine aggregates in diffusion creep and concluded that long range Si^{4+} grain boundary diffusion is not required for the diffusive mass transfer [see also *Wheeler*, 1992]. The same situation applies to the K-feldspar-albite system of this study: for chemical homogenization and local mass transfer by diffusion creep, Na^+ and K^+ transport is sufficient and rapid at the temperature conditions of our experiments.

The EBSD data lend further support to the interpretation of diffusion (dissolution-precipitation) creep as the dominant deformation mechanism in the fine-grained K-feldspar. Numerical models have suggested that anisotropic dissolution and growth rates during diffusion creep can result in a crystallographic preferred orientation, in which the crystallographic direction of faster dissolution/growth rate ends up aligned with the instantaneous stretching axis during viscous flow [*Bons and den Brok*, 2000]. The alignment of (010) planes with the shear band boundaries and of the [100] axes with the stretching axis can be explained as a shape fabric produced by oriented growth during melt flow and diffusion creep. The [100] axis of K-feldspar has been interpreted as the direction of faster growth during anisotropic dissolution and precipitation in a number of studies [*Menegon et al.*, 2008]. Thus, the well-developed crystallographic preferred orientation of the nucleated, chemically homogeneous euhedral feldspar grains along fractures (Figure 7) can be explained by rigid body rotation and anisotropic growth. Anisotropic dissolution and precipitation has been invoked as a CPO-forming mechanism for other minerals (clinopyroxene [*Godard and Van Roermund*, 1995], quartz [*Takeshita and Hara*, 1998], albite [*Heidelbach et al.*, 2000], amphibole [*Pearce et al.*, 2011], and in the presence of melt [*John and Stünitz*, 1997]).

4.3. Strength of Samples in the Presence of Melt

As observed by, e.g., *Arzi* [1978], *van der Molen and Paterson* [1979], and *Rutter and Neumann* [1995] (for a review see *Rosenberg and Handy* [2001]), the presence of melt in granitic rocks typically causes a dramatic weakening at melt fractions of 20–30% [*Arzi*, 1978; *van der Molen and Paterson*, 1979]. The perthite single crystals in this study do not show dramatic weakening in the presence of melt compared to creep experiments on solid plagioclase samples: the flow stresses at 1.0 and 1.5 GPa are between 300 and 400 MPa, similar to polycrystalline solid albite material at the same temperature and strain rate conditions [*Tullis and Yund*, 1985; *Tullis et al.*, 1990], and higher than fine-grained plagioclase at 900°C and 1 GPa [*Stünitz and Tullis*, 2001]. The fact that the strength of the single-crystal material does not decrease to values observed for melt-controlled deformation is probably due to the fact that melt fractions are small (≤ 5 vol %). Melt interconnectivity and migration is expected at melt fractions greater than $\Phi_{vol} = 0.07$ [*Vigneresse et al.*, 1996; *Rosenberg and Handy*, 2005; *Menegon et al.*, 2011]. The melt in our samples is not simply connected (i.e., islands of solid material exist in melt films along the fracture surfaces; Figures 6 and 7). Simple connectivity

appears to be a prerequisite for substantial mechanical weakening, whereas for melt segregation nonsimple connectivity appears to be sufficient. In the high-strain experiments of *Zimmerman et al.* [1999] and *Bruhn et al.* [2000], where they observed melt interconnectivity even at small melt fractions (especially in fine-grained portions of the material) [*Wark and Watson* 2000; *Bruhn et al.*, 2000], the melt remained nonsimply connected, and the mechanical effect was not dramatic. Thus, in our samples, the bulk stress is to a large extent supported by the solid framework of intact crystals and by clast material and it is likely that many clast interfaces without melt films in the fractured regions partly control the mechanical behavior of the samples rather than the presence of melt.

The pressure dependence of deformation at 900°C is pronounced (Figure 3). The stress-strain curves show a decrease of peak strength with increasing confining pressure: Samples deformed at 900°C and 0.75 GPa show high peak stresses followed by pronounced weakening, whereas those deformed at 1.5 GPa show no peak stress and a lower steady state flow stress after 5% strain (Figure 3). Microstructural observations indicate that at peak stress the 0.75 GPa experiments contain almost no melt, whereas the 1.5 GPa samples show a higher melt fraction at peak stress. One explanation for the steady state deformation and initially lower flow stresses at 1.5 GPa may be that the equilibrium H_2O content of the melt is higher at the higher confining pressure [*Behrens et al.*, 2001], and the viscosity of the melt decreases by at least 1 order of magnitude with the increased H_2O content [*Johannes and Holtz*, 1996]. The lower viscosity causes more efficient wetting of the grain boundaries leading to more effective transport during diffusion creep, and thus an increase in local strain rates in the cracked domains containing melt. Thus, at high confining pressure, the onset of viscous deformation occurs relatively early because of the initial higher melt fraction (although at higher pressure the total finite amount of melt is expected to be lower than at low pressure because of the higher H_2O content of the melt) and the viscous strain rates are expected to be higher. At lower confining pressures, the pronounced weakening behavior is explained by progressive melt formation with time and more cracking with increasing strain.

4.3.1. Geological Implications

The role of deformation in melt segregation and extraction in the continental crust has been emphasized by, e.g., *Brown* [1994, 2010]; *Weinberg* [1999]; *Rosenberg and Berger* [2001]; *Sawyer* [2001]; *Marchildon and Brown* [2002]. However, the importance of deformation for the melting process itself has only recently been proposed by, e.g., *Tumarkina et al.* [2011]. The processes of cracking and dilatancy described in this study are potentially important for the generation of H_2O-undersaturated melts and fluid-absent melting is one of the most efficient ways to accommodate the necessary volume increase during melting. As H_2O-undersaturated melting typically occurs in metapelitic and quartzofeldspathic rocks at high temperatures in nature, the traces of initial cracking are likely to be obscured by viscous deformation. In turn, some cracking may be enhanced by the formation of low-viscosity melts from pore pressure effects [e.g., *Davidson et al.*, 1994]. Thus, cracking and melt formation may be intimately linked processes in crustal settings.

The mechanical weakening of the material by diffusion creep is caused by melt-enhanced transport properties of the fine-grained domains originally produced by cracking. This effect may help to initiate deformation of melting rocks, even at very small melt percentages, which do not lead to the formation of typical migmatite structures. Melt-enhanced diffusion creep has been described for mantle and mafic rocks [e.g., *Hirth and Kohlstedt*, 1995a, 1995b] but has not been observed so far in crustal lithologies. This study shows that in feldspar-rich compositions, it is likely that this process is active. Small melt percentages may weaken the rock substantially by inducing melt-assisted diffusion creep even if they do not lead to a complete breakdown of the load-supporting framework in crustal rocks. Due to the viscous deformation at elevated temperatures and melt-induced weakening, the preservation potential of initially brittle structures in melting rocks is not very good. The detection of such microstructures would be important for identifying the interplay between cracking and melt-enhanced diffusion creep in natural crustal rocks.

5. Conclusions

High-temperature (700°C and 900°C) and high-pressure (0.75 to 1.5 GPa) deformation experiments conducted in a solid medium deformation apparatus on perthitic K-feldspar single crystals and powder samples show brittle and semibrittle deformation, dependent on temperature. The transition between brittle and semibrittle deformation occurs in the temperature interval of 700°C to 900°C: At 700°C

deformation of K-feldspar is accommodated by brittle shear fractures without formation of melt, whereas deformation at 900°C is dominated by simultaneous cracking and melting. The relatively high flow stresses (considering that a melt is present) during deformation are consistent with microstructural observations of isolated and not simply connected melt domains of variable composition at low melt fractions of less than 5%. At 900°C, the deformation should be considered as semibrittle.

The partial melts formed at 900°C are H_2O undersaturated. The sources of H_2O are very small amounts of free fluid (e.g., fluid inclusions) and white mica dehydration. Chemical homogenization of the solid feldspars (albite and K-feldspar) occurs in the immediate vicinity of fractured and melt-bearing domains producing variable, intermediate compositions, largely by replacement of fine-grained gouge material by dissolution-precipitation processes.

Hydrostatically heat-treated samples at 900°C do not show any partial melting or chemical homogenization even although temperatures were ~200°C above the solidus. The fact that melt formation is suppressed in the hydrostatic experiments is likely due to the local pressure increase that would occur during the melt-forming reaction, because of the solidus curve with a positive Clausius-Clapeyron slope (typical for H_2O-undersaturated melts). In contrast, in the deformation experiments, cracking produces dilatancy, local pressure drops around the cracks, and thus enhanced melt formation.

Melt along fractures accommodates displacement by viscous processes; however, it does not dramatically weaken the samples. The dissolution precipitation processes are most likely enhanced by the presence of melt in fractured regions. As no crystal plastic deformation features are observed in these samples, viscous deformation in the fine-grained fault gouge is most likely accommodated by diffusion creep (grain boundary sliding and dissolution-precipitation creep). This experimental study highlights the strong interrelationships between brittle fracturing, melting, and subsequent semibrittle deformation in crustal minerals (feldspar) at elevated pressures and temperatures.

References

Adams, B. L., S. I. Wright, and K. Kunze (1993), Orientation imaging: The emergence of a new microscopy, *Metall. Trans. A*, *24*(4), 819–831.

Alling, H. (1938), Plutonic perthites, *J. Geol.*, *46*, 142–165.

Arzi, A. A. (1978), Critical phenomena in the rheology of partially melted rocks, *Tectonophysics*, *44*, 173–184.

Beaumont, C., R. A. Jamieson, M. H. Nguyen, and B. Lee (2001), Himalayan tectonics explained by extrusion of a low-viscosity crustal channel coupled to focused surface denudation, *Nature*, *414*(6865), 738–742, doi:10.1038/414738a.

Behrens, H. (1995), Determination of water solubilities in high-viscosity melts: An experimental study on NaAlSi3O8 and KAlSi3O8 melts, *Eur. J. Mineral.*, *7*, 905–920.

Behrens, H., M. Meyer, F. Holtz, D. Benne, and M. Nowak (2001), The effect of alkali ionic radius, temperature, and pressure on the solubility of water in MAlSi3O8 melts (M = Li, Na, K, Rb), *Chem. Geol.*, *174*, 275–289.

Bell, T. H., and S. E. Johnson (1989), The role of deformation partitioning in the deformation and recrystallization of plagioclase and K-feldspar in the Woodroffe Thrust mylonite zone, central Australia, *J. Metamorph. Geol.*, *7*, 151–168.

Bons, P. D., and B. den Brok (2000), Crystallographic preferred orientation development by dissolution-precipitation creep, *J. Struct. Geol.*, *22*, 1713–1722.

Brady, J. B., and R. A. Yund (1983), Interdiffusion of K and Na in alkali feldspars: Homogenization experiments, *Am. Mineral.*, *68*, 106–111.

Brown, M. (1994), The generation, segregation, ascent and emplacement of granite magma: The migmatite-to-crustally-derived granite connection in thickened orogens, *Earth Sci. Rev.*, *36*(1-2), 83–130, doi:10.1016/0012-8252(94)90009-4.

Brown, M. (2007), Crustal melting and melt extraction, ascent and emplacement in orogens: Mechanisms and consequences, *J. Geol. Soc.*, *164*(1993), 709–730.

Brown, M. (2010), The spatial and temporal patterning of the deep crust and implications for the process of melt extraction, *Philos. Trans. A Math Phys. Eng. Sci.*, *368*(1910), 11–51, doi:10.1098/rsta.2009.0200.

Brown, M., and G. S. Solar (1998), Shear-zone systems and melts: Feedback relations and self-organization in orogenic belts, *J. Struct. Geol.*, *20*(2/3), 211–277.

Bruhn, D., N. J. Groebner, and D. L. Kohlstedt (2000), An interconnected network of core-forming melts produces by shear deformation, *Nature*, *403*, 883–886.

Bussod, G. Y., and J. M. Christie (1991), Textural development and melt topology in spinel lherzolite experimentally deformed at hypersolidus conditions, *J. Petrol.*, *2*, (Special Lherzolite Issue), 17–39.

Christoffersen, R., R. A. Yund, and J. Tullis (1983), Inter-diffusion of K and Na in alkali feldspars: Diffusion couple experiments, *Am. Mineral.*, *68*, 1126–1133.

Clark, M. K., and L. H. Royden (2000), Topographic ooze: Building the eastern margin of Tibet by lower crustal flow, *Geology*, *28*(8), 703–706, doi:10.1130/0091-7613(2000)28<703.

Coggon, R., and T. J. B. Holland (2002), Mixing properties of phengitic micas and revised garnet–phengite thermobarometers, *J. Metamorph. Geol.*, *20*, 683–696.

Collins, W. J., and E. W. Sawyer (1996), Pervasive granitoid magma transfer through the lower–middle crust during non-coaxial compressional deformation, *J. Metamorph. Geol.*, *14*(1992), 565–579.

Connolly, J. A. D. (2009), The geodynamic equation of state: What and how, *Geochem. Geophys. Geosyst.*, *10*, Q10014, doi:10.1029/2009GC002540.

Cooper, R. F. (1990), Differential stress-induced melt migration: An experimental approach, *J. Geophys. Res.*, *95*(B5), 6979, doi:10.1029/JB095iB05p06979.

Cooper, R. F., and D. L. Kohlstedt (1984a), Sintering of olivine and olivine-basalt aggregates, *Phys. Chem. Miner.*, *11*, 5–16.

Cooper, R. F., and D. L. Kohlstedt (1984b), Solution-precipitation enhanced diffusional creep of partially molten olivine-basalt aggregates during hot-pressing, *Tectonics*, *107*, 207–233.

Cooper, R. F., D. L. Kohlstedt, and K. Chyung (1989), Solution-precipitation enhanced creep in solid-liquid aggregates which display a non-zero dihedral angle, *Acta Metall.*, *37*(7), 1759–1771, doi:10.1016/0001-6160(89)90061-8.

Daines, M. J., and D. L. Kohlstedt (1997), Influence of deformation on melt topology in peridotites, *J. Geophys. Res.*, *107*, 10,257–10,271.

Davidson, C., S. M. Schmid, and L. S. Hollister (1994), Role of melt during deformation in the deep crust, *Terra Nova*, *6*, 133–142.

De Ronde, A., and H. Stünitz (2007), Deformation-enhanced reaction in experimentally deformed plagioclase-olivine aggregates, *Contrib. Mineral. Petrol.*, *153*, 699–717.

De Ronde, A., R. Heilbronner, H. Stünitz, and J. Tullis (2004), Spatial correlation of deformation and mineral reaction in experimentally deformed plagioclase-olivine aggregates, *Tectonophysics*, *389*(1-2), 93–109.

De Ronde, A., H. Stünitz, J. Tullis, and R. Heilbronner (2005), Reaction-induced weakening of plagioclase-olivine composites, *Tectonophysics*, *409*(1–4), 85–106.

Debat, P., J. C. Soula, L. Kubin, and J. L. Vidal (1978), Optical studies of natural deformation microstructures in feldspar (gneiss and pegmatites from Occitania southern France), *Lithos*, *11*, 133–145.

Dell'Angelo, L. N., and J. Tullis (1988), Experimental deformation of partially melted granitic aggregates, *J. Metamorph. Geol.*, *6*(4), 495–515, doi:10.1111/j.1525-1314.1988.tb00436.x.

Dell'Angelo, L. N., J. Tullis, and R. A. Yund (1987), Transition from dislocation creep to melt-enhanced diffusion creep in fine-grained granitic aggregates, *Tectonophysics*, *139*, 325–332.

Dimanov, A., G. Dresen, and R. Wirth (1998), High-temperature creep of partially molten plagioclase aggregates, *J. Geophys. Res.*, *103*(B5), 9651–9664, doi:10.1029/97JB03742.

Dimanov, A., R. Wirth, and G. Dresen (2000), The effect of melt distribution on the rheology of plagioclase rocks, *Tectonophysics*, *328*, 307–327.

Fitz Gerald, J. D., and A. C. McLaren (1982), The microstructures of microcline from some granitic rocks and pegmatites, *Contrib. Mineral. Petrol.*, *80*, 219–229.

Fitz Gerald, J. D., and H. Stünitz (1993), Deformation of granitoids at low metamorphic grade. I. Reactions and grain size reduction, *Tectonophysics*, *221*, 269–297.

Flynn, G. W., and W. J. A. Powell (1988), *Cutting and Polishing Optical and Electronic Materials*, 2nd ed., Adam Hilger, Bristol, U. K.

Godard, G., and H. L. M. van Roermund (1995), Deformation-induced clinopyroxene fabrics from eclogites, *J. Struct. Geol.*, *17*, 1425–1443.

Greenwood, J. P., and P. C. Hess (1998), Congruent melting kinetics of albite: Theory and experiment, *J. Geophys. Res.*, *103*(98), 29,815–29,828.

Hadizadeh, J., and J. Tullis (1992), Cataclastic flow and semi-brittle deformation of anorthosite, *J. Struct. Geol.*, *14*(1), 57–63.

Heidelbach, F., A. Post, and J. Tullis (2000), Crystallographic preferred orientation in albite samples deformed experimentally by dislocation and solution precipitation creep, *J. Struct. Geol.*, *22*(11-12), 1649–1661, doi:10.1016/S0191-8141(00)00072-9.

Hess, P. C. (1994), Thermodynamics of thin fluid films, *J. Geophys. Res.*, *99*(93), 7219–7229.

Hielscher, R., and H. Schaeben (2008), A novel pole figure inversion method: Specification of the MTEX algorithm, *J. Appl. Crystallogr.*, *41*(6), 1024–1037.

Hirth, G., and D. L. Kohlstedt (1995a), Experimental constraints on the dynamics of the partially molten upper mantle: Deformation in the diffusion creep regime, *J. Geophys. Res.*, *100*, 1981–2001.

Hirth, G., and D. L. Kohlstedt (1995b), Experimental constraints on the dynamics of the partially molten upper mantle: 2. Deformation in the dislocation creep regime, *J. Geophys. Res.*, *100*, 15,441–15,449.

Hirth, G., and D. L. Kohlstedt (2003), Inside the subduction Factory, in *Rheology of the Upper Mantle and the Mantle Wedge: A View From the Experimentalists*, Geophys. Monogr. Ser., vol. 138, edited by J. Eiler, pp. 83–105, Am. Geophys. Soc., Washington, D. C.

Holland, T. J. B., and R. Powell (1998), An internally-consistent thermodynamic dataset for phases of petrological interest, *J. Metamorph. Geol.*, *16*, 309–344.

Holtz, F., M. Pichavant, P. Barbey, and W. Johannes (1992), Effects of H2O on liquidus phase relations in the haplogranite system at 2 and 5 kbar, *Am. Mineral.*, *77*, 1223–1241.

Holtzman, B. K., and D. L. Kohlstedt (2007), Stress-driven melt segregation and strain partitioning in partially molten rocks: Effects of stress and strain, *J. Petrol.*, *48*(12), 2379–2406, doi:10.1093/petrology/egm065.

Holtzman, B. K., N. J. Groebner, M. E. Zimmerman, S. B. Ginsberg, and D. L. Kohlstedt (2003a), Stress-driven melt segregation in partially molten rocks, *Geochem. Geophys. Geosyst.*, *4*, 8607, doi:10.1029/2001GC000258.

Holtzman, B. K., D. L. Kohlstedt, M. E. Zimmerman, F. Heidelbach, T. Hiraga, and J. W. Hustoft (2003b), Supplemental online material to melt segregation and strain partitioning: Implications for seismic anisotropy and mantle flow, *Science*, *1*, 1–9.

Jin, Z.-M., H. W. Green, and Y. Zhou (1994), Melt topology in partially molten mantle peridotite during ductile deformation, *Lett. Nat.*, *372*, 164–166.

Johannes, W., and F. Holtz (1996), *Petrogenesis and Experimental Petrology of Granitc Rocks*, Springer, Berlin.

John, B. E., and H. Stünitz (1997), Evidence for magma fracturation and small scale melt segregation during pluton emplacement, in *Granites: From Segregation of Melt to Emplacement Fabric*, edited by J. L. Bouchez, D. H. Hutton, and E. S. Stephens, pp. 55–75, Kluwer Acad., Dordrecht, Netherlands.

King, D. S. H., M. E. Zimmerman, and D. L. Kohlstedt (2010), Stress-driven melt segregation in partially molten olivine-rich rocks deformed in torsion, *J. Petrol.*, *51*, 612–626, doi:10.1093/petrology/egp062.

King, J., N. Harris, T. Argles, R. Parrish, and H. Zhang (2011), Contribution of crustal anatexis to the tectonic evolution of Indian crust beneath southern Tibet, *Geol. Soc. Am. Bull.*, *123*(1-2), 218–239, doi:10.1130/B30085.1.

Kohlstedt, D. L. (1992), Structure, rheology and permeability of partially molten rocks at low melt fractions, in *Mantle Flow and Melt Generation at Mid-Ocean Ridges*, edited by J. Philipps-Morgan, D. Blackman, and J. Sinton, pp. 103–121, AGU, Washington, D. C.

Kohlstedt, D. L., and B. K. Holtzman (2009), Shearing melt out of the Earth: An experimentalist's perspective on the influence of deformation on melt extraction, *Annu. Rev. Earth Planet. Sci.*, *37*(1), 561–593, doi:10.1146/annurev.earth.031208.100104.

Kohlstedt, D. L., and M. E. Zimmerman (1996), Rheology of partially molten mantle rocks, *Annu. Rev. Earth Planet. Sci.*, *24*, 41–62.

Kohlstedt, D. L., B. Evans, and S. J. Mackwell (1995), Strength of the lithosphere: Constraints imposed by laboratory experiments, *J. Geophys. Res.*, *100*, 17,587–17,602.

Kohlstedt, D. L., M. E. Zimmerman, and S. J. Mackwell (2009), Stress-driven melt segregation in partially molten feldspathic rocks, *J. Petrol.*, *51*(1-2), 9–19, doi:10.1093/petrology/egp043.

Lexa, O., K. Schulmann, V. Janoušek, P. Štípská, A. Guy, and M. Racek (2011), Heat sources and trigger mechanisms of exhumation of HP granulites in Variscan orogenic root, *J. Metamorph. Geol.*, *29*(1), 79–102, doi:10.1111/j.1525-1314.2010.00906.x.

Luth, W. C., R. H. Jahnes, and O. F. Tuttle (1964), The granite system at pressure of 4 to 10 kilobars, *J. Geophys. Res.*, *69*, 759–773.

Marchildon, N., and M. Brown (2002), Grain-scale melt distribution in two contact aureole rocks: Implications for controls on melt localization and deformation, *J. Metamorph. Geol.*, *20*(4), 381–396, doi:10.1046/j.1525-1314.2002.00376.x.

Mecklenburgh, J., and E. H. Rutter (2003), On the rheology of partially molten synthetic granite, *J. Struct. Geol.*, *25*(10), 1575–1585, doi:10.1016/S0191-8141(03)00014-2.

Menegon, L., G. Pennacchioni, and R. Spiess (2008), Dissolution-precipitation creep of K-feldspar in mid-crustal granite mylonites, *J. Struct. Geol.*, *30*, 565–579.

Menegon, L., P. Nasipuri, H. Stünitz, H. Behrens, and E. J. K. Ravna (2011), Dry and strong quartz during deformation of the lower crust in the presence of melt, *J. Geophys. Res.*, *116*(B10), 1–23, doi:10.1029/2011JB008371.

Misra, S., L. Burlini, and J.-P. Burg (2009), Strain localization and melt segregation in deforming metapelites, *Phys. Earth Planet. Inter.*, *177*(3-4), 173–179, doi:10.1016/j.pepi.2009.08.011.

Morse, S. A. (1970), Alkali feldspar with water at 5 kb pressure, *J. Pet. Sci. Technol. Eng.*, *11*, 221–253.

Parsons, R., J. W. Hustoft, D. L. Holtzman, D. L. Kohlstedt, and J. P. Morgan (2004), Stress-driven melt segregation and organization in partially molten rocks; III, Annealing experiments and surface tension-driven redistribution of melt, *Eos Trans. AGU*, AGU 2004 Fall Meet. 85 (47, Suppl.), Abstract V21A - 0599.

Pearce, M. A., J. Wheeler, and D. J. Prior (2011), Relative strength of mafic and felsic rocks during amphibolite facies metamorphism and deformation, *J. Struct. Geol.*, *33*, 662–675.

Pharr, G. M., and M. F. Ashby (1983), On creep enhanced by a liquid phase, *Acta Metall.*, *31*, 129–138.

Putnis, A. (2002), Mineral replacement reactions: From macroscopic observations to microscopic mechanisms, *Mineral. Mag.*, *66*, 689–708.

Raj, R. (1982), Creep in polycrystalline aggregates by matter transport through a liquid phase, *J. Geophys. Res.*, *87*, 4731–4739.

Rosenberg, C. L., and A. Berger (2001), Syntectonic melt pathways in granitic gneisses, and melt-induced transitions in deformation mechanisms, *Phys. Chem. Earth*, *26*(4), 287–293.

Rosenberg, C. L., and M. R. Handy (2001), Mechanisms and orientation of melt segregation paths during pure shearing of a partially molten rock analog (norcamphor ± benzamide), *J. Struct. Geol.*, *23*, 1917–1932.

Rosenberg, C. L., and M. R. Handy (2005), Experimental deformation of partially melted granite revisited: Implications for the continental crust, *J. Metamorph. Geol.*, *23*, 19–28, doi:10.1111/j.1525-1314.2005.00555.x.

Royden, L. H., B. C. Burchfiel, and R. D. van der Hilst (2008), The geological evolution of the Tibetan Plateau, *Science* (New York, N.Y.), *321*(5892), 1054–1058, doi:10.1126/science.1155371.

Rutter, E. H., and D. H. K. Neumann (1995), Experimental deformation of partially molten Westerly granite under fluid-absent conditions, with implications for the extraction of granitic magmas, *J. Geophys. Res.*, *100*, 15,697–15,715.

Sacerdoti, M., H. Labernardiere, and M. Gandais (1980), Transmission electron microscope (TEM) study of geologically deformed potassic feldspar, *Bull. Mineral.*, *103*, 148–155.

Sawyer, E. W. (2001), Melt segregation in the continental crust: Distribution and movement of melt in anatectic rocks, *J. Metamorph. Geol.*, *19*(3), 291–309, doi:10.1046/j.0263-4929.2000.00312.x.

Schulmann, K., O. Lexa, P. Štípská, M. Racek, L. Tajčmanová, J. Konopásek, J.-B. Edel, A. Peschler, and J. Lehmann (2008), Vertical extrusion and horizontal channel flow of orogenic lower crust: Key exhumation mechanisms in large hot orogens?, *J. Metamorph. Geol.*, *26*(2), 273–297, doi:10.1111/j.1525-1314.2007.00755.x.

Scott, T., and D. L. Kohlstedt (2006), The effect of large melt fraction on the deformation behavior of peridotite, *Earth Planet. Sci. Lett.*, *246*, 177–187, doi:10.1016/j.epsl.2006.04.027.

Slagstad, T. (2005), Formation, crystallization, and migration of melt in the Mid-orogenic crust: Muskoka domain migmatites, Grenville Province, Ontario, *J. Petrol.*, *46*(5), 893–919, doi:10.1093/petrology/egi004.

Smith, J. V., and W. L. Brown (1988), *Feldspar Minerals 1: Crystal Structures, Physical, Chemical and Microtextural Properties*, vol. 1, 2nd ed., Springer, Berlin.

Stevenson, J. (1989), Spontaneous small-scale melt segregation in partial melts undergoing deformation, *Geophys. Res. Lett.*, *16*(9), 1067–1070.

Stünitz, H., and J. Tullis (2001), Weakening and strain localization produced by syn-deformational reaction of plagioclase, *Int. J. Earth Sci.*, *90*(1), 136–148, doi:10.1007/s005310000148.

Stünitz, H., J. D. Fitz Gerald, and J. Tullis (2003), Dislocation generation, slip systems, and dynamic recrystallization in experimentally deformed plagioclase single crystals, *Tectonophysics*, *372*(3-4), 215–233, doi:10.1016/S0040-1951(03)00241-5.

Sundberg, M., and R. F. Cooper (2008), Crystallographic preferred orientation produced by diffusional creep of harzburgite: Effects of chemical interactions among phases during plastic flow, *J. Geophys. Res.*, *113*, 1–16, doi:10.1029/2008JB005618.

Takei, Y., and B. K. Holtzman (2009), Viscous constitutive relations of solid-liquid composites in terms of grain boundary contiguity: 1. Grain boundary diffusion control model, *J. Geophys. Res.*, *114*, B06205, doi:10.1029/2008JB005850.

Takeshita, T., and I. Hara (1998), C-axis fabrics and microstructures in a recrystallized quartz vein deformed under fluid-rich greenschist conditions, *J. Struct. Geol.*, *20*, 417–431.

Thompson, J. B. J., and D. R. Waldbaum (1969), Mixing properties of sanidine crystalline solutions: III. Calculations based on two-phase data, *Am. Mineral.*, *54*, 811–838.

Tullis, J. (1983), Deformation of feldspar, *Rev. Mineral.*, *2*, 297–323.

Tullis, J. (2002), Deformation of granitic rocks: Experimental studies and natural examples, *Rev. Mineral. Geochem.*, *51*(1), 51–95.

Tullis, T. E., and J. Tullis (1986), Experimental rock deformation techniques, in *Mineral and Rock Deformation: Laboratory Studies, Geophys. Monogr. Ser.*, edited by B. Hobbs and H. Heard, AGU, Washington, D. C.

Tullis, J., and R. A. Yund (1977), Experimental deformation of dry Westerly granite, *J. Geophys. Res.*, *82*, 5705–5718.

Tullis, J., and R. A. Yund (1985), Dynamic recrystallization of feldspar: A mechanism for ductile shear zone formation, *Geology*, *13*, 238–241, doi:10.1130/0091-7613(1985)13<238.

Tullis, J., and R. A. Yund (1987), Transition from cataclastic flow to dislocation creep of feldspar: Mechanisms and microstructures, *Geology*, *15*, 606–609, doi:10.1130/0091-7613(1987)15<606.

Tullis, J., and R. A. Yund (1991), Diffusion creep in feldspar aggregates: Experimental evidence, *J. Struct. Geol.*, *13*, 987–1000.

Tullis, J., and R. A. Yund (1992), The brittle-ductile transition in feldspar aggregates: An experimental study, in *Fault Mechanics and Transport Properties of Rock*, edited by B. Evans and T. Wong, Academic Press, London, U. K.

Tullis, J., and R. A. Yund (1996), Deformation-enhanced fluid- distribution in feldspar aggregates and implications for ductile shear zones, *Geology*, *24*, 63–66.

Tullis, J., L. N. Dell'Angelo, and R. A. Yund (1990), Ductile shear zones from brittle precursors in feldspathic rocks: The role of dynamic recrystallization, in *The Brittle-Ductile Transition in Rocks: The Heard Volume*, *Geophys. Monogr. Ser.*, vol. 56, edited by A. G. Duba et al., pp. 67–81, AGU, Washington, D. C.

Tumarkina, E., S. Misra, L. Burlini, and J. A. D. Connolly (2011), An experimental study of the role of shear deformation on partial melting of a synthetic metapelite, *Tectonophysics*, *503*(1-2), 92–99, doi:10.1016/j.tecto.2010.12.004.

van der Molen, I., and M. S. Paterson (1979), Experimental deformation of partially-melted granite, *Contrib. Mineral. Petrol.*, *70*, 299–318.

Vidal, J. L., L. Kubin, P. Debat, and J. C. Soula (1980), Deformation and dynamic recrystallization of K feldspar augen in orthogneiss from Montagne Noire, Occitania, southern France, *Lithos*, *13*, 247–255.

Vigneresse, J. L. (1995a), Control of granite emplacement by regional deformation, *Tectonophysics*, *249*(3-4), 173–186, doi:10.1016/0040-1951(95)00004-7.

Vigneresse, J. L. (1995b), Crustal regime of deformation and ascent of granitic magma, *Tectonophysics*, *249*(3-4), 187–202, doi:10.1016/0040-1951(95)00005-8.

Vigneresse, J. L., P. Barbey, and M. Cuney (1996), Rheological transitions during partial melting and crystallization with application to felsic magma segregation and transfer, *J. Petrol.*, *37*(6), 1579–1600.

Wark, D. A., and B. E. Watson (2000), Effect of grain size on the distribution and transport of deep-seated fluids and melts, *Geophys. Res. Lett.* *27*, 2029–2032.

Weinberg, R. F. (1999), Mesoscale pervasive felsic magma migration: Alternatives to dyking, *Lithos*, *46*(3), 393–410, doi:10.1016/S0024-4937(98)00075-9.

Wheeler, J. (1992), Importance of pressure solution and coble creep in the deformation of polymineralic rocks, *J. Geophys. Res.*, *97*(B4), 4579–4586, doi:10.1029/91JB02476.

White, J. C., and C. K. Mawer (1988), Dynamic recrystallization and associated exsolution in perthites: Evidence of deep crustal thrusting, *J. Geophys. Res.*, *93*, 325–337.

Wickham, S. M. (1987), The segregation and emplacement of granitic magmas, *J. Geol. Soc.*, *144*(2), 281–297, doi:10.1144/gsjgs.144.2.0281.

Willaime, C., and M. Gandais (1972), Study of the exsolution in alkali feldspars. Calculation of elastic stresses inducing periodic twins, *Phys. Status Solid A Appl. Res.*, *9*, 529–539.

Willaime, C., W. L. Brown, and M. Gandais (1973), An electron microscopic and X-ray study of a complex exsolution textures in a cryptoperthitic alkali feldspar, *J. Mater. Sci.*, *8*, 461–466.

Willaime, C., J. M. Christie, and D. Mainprice (1979), Experimental deformation of K-feldspar single crystals, *Bull. Mineral.*, *102*, 168–177.

Yund, R. A. (1983), Diffusion in feldspar, in *Mineralogical Society of America Reviews in Mineralogy*, vol. 2, rev., edited by P. H. Ribbe, pp. 203–222, Feldspars, Washington, D. C.

Zimmerman, M. E., and D. L. Kohlstedt (2004), Rheological properties of partially molten lherzolite, *J. Struct. Geol.*, *45*, 275–298.

Zimmerman, M. E., S. Zhang, D. L. Kohlstedt, and S. Karato (1999), Melt distribution in mantle rocks deformed in shear, *Geophys. Res. Lett.*, *26*(10), 1505–1508, doi:10.1029/1999GL900259.